

Copyright Undertaking

This thesis is protected by copyright, with all rights reserved.

By reading and using the thesis, the reader understands and agrees to the following terms:

1. The reader will abide by the rules and legal ordinances governing copyright regarding the use of the thesis.
2. The reader will use the thesis for the purpose of research or private study only and not for distribution or further reproduction or any other purpose.
3. The reader agrees to indemnify and hold the University harmless from and against any loss, damage, cost, liability or expenses arising from copyright infringement or unauthorized usage.

If you have reasons to believe that any materials in this thesis are deemed not suitable to be distributed in this form, or a copyright owner having difficulty with the material being included in our database, please contact lbsys@polyu.edu.hk providing details. The Library will look into your claim and consider taking remedial action upon receipt of the written requests.

Aerodynamic and Vibroacoustic Noise of Small Axial-flow Fans: Analysis and Control

Department of Mechanical Engineering

CHONG Tat Lung

Dissertation submitted for the partial fulfilment for the

Degree of Master of Philosophy

THE HONG KONG POLYTECHNIC UNIVERSITY

2002



Pao Yue-Kong Library
PolyU • Hong Kong

Table of Contents

List of figures	2
Abstract	5
Chapter 1: Introduction	8
1.1 Literature review of fan noise and its control	8
1.2 Fan noise mechanisms.....	14
1.2.1 Vibrational noise	14
1.2.2 Gutin noise	15
1.2.3 Unsteady flow noise.....	17
1.3 Directivity of isolated impeller noise.....	19
1.4 Objectives and methodology of this project.....	22
Chapter 2: Flow measurement and analysis.....	25
2.1 Velocity measurement by Pitot-static tube	26
2.2 Velocity triangle analysis.....	27
2.3 Hot wire measurement	30
2.4 Flow field analysis	35
Chapter 3: Noise and vibration measurement	38
3.1 Calibration of two microphones.....	39
3.2 Application to duct acoustics measurement.....	42
3.3 Tachometer-triggered data acquisition system.....	47
3.4 Basic characters of the impeller noise.....	49
Chapter 4: Acoustic analysis.....	52
4.1 Signal calibration and filtering.....	54
4.2 Correlation studies	55
4.3 One-microphone method.....	57
4.4 Variation with rpm	60
Chapter 5: Noise abatement	64
5.1 Introductory remarks.....	64
5.2 Effect of changing the guidevane in the hair dryer	65
5.3 Effect of changing the impeller tip clearance	67
5.4 Effect of adding perforated sheet	69
Chapter 6: Discussions.....	71
Chapter 7: Conclusions	74
Acknowledgements	75
References	76
Appendix	80

List of figures

Figure 1.1	Illustration of the conceptual dipole as a limiting process of two monopoles, and the directivity of the dipole source.	P.80
Figure 1.2	Directivity of thickness noise.	P.80
Figure 1.3	Noise generated by the steady loading on rotating blades. (a) shows the separation of loading on each blade cross section, (b) is the directivity of noise caused by the rotated thrust force, (c) shows the directivity of the torque noise, (d) is the directivity of the total steady loading noise.	P.81
Figure 1.4	Noise radiated by the rigid-body vibration of the motor-fan assembly. (a) is the front view of the fan blades with the assembly vibration following an elliptic path (exaggerated), (b) shows the directivity of the far field sound on the side view.	P.81
Figure 1.5	Photographs of the sample hair dryer fan used in the study. (a) is the complete hair dryer fan, (b) is the isolated impeller driven by the motor housed in a metal cylinder.	P.82
Figure 2.1	The Pitot-tube measurement of the flow through a tube. (a) illustrate the principle of the Pitot-static tube, (b) shows the arrangements of the measurement points over a circular cross section.	P.83
Figure 2.2	The velocity triangle analysis for a fan impeller.	P.83
Figure 2.3	The x-wire probe.	P.84
Figure 2.4	X-wire measurement for the axial and circumferential components of the absolute flow velocity downstream of the impeller.	P.84
Figure 2.5	Distribution of X-wire measured average flow velocity in axial (U) and circumferential (V) directions for two values of tip clearance: 1mm (solid squares) and 2mm (open squares).	P.85
Figure 2.6	Distribution of local average of the axial flow velocity (solid curves, viewed from ground) and its standard deviation (vertical bars, over 500 cycles of measurements). The observation point has the angular position of Φ fixed to the impeller and the radial position is marked on each graph.	P.86
Figure 2.7	Distribution of local average of the circumferential velocity and its standard deviation.	P.87
Figure 3.1	The schematic diagram of microphone calibration.	P.88

Figure 3.2	The results of microphone calibration by the microphone-swapping method inside a duct. (a) is the amplitude ratio, (b) is the phase angle difference.	P.88
Figure 3.3	The experimental set-up for the duct acoustics project.	P.89
Figure 3.4	The comparison of theoretical prediction (solid curves) and experimental data (open squares) of the dispersion relation for sound propagation through a duct with one flexible wall. The experiment were conducted by the chirp sound source. (a) is the experimental data over the whole frequency range, (b) and (c) are, respectively, the zoom-in views of the data compared with theoretical predictions for the two frequency regions in which the wave speed is subsonic and supersonic.	P.89
Figure 3.5	The schematic diagram of the experiment.	P.90
Figure 3.6	The LabVIEW code controlling the data acquisition process. The top is the front panel and the lower picture is the diagram of the code.	P.91
Figure 3.7	Example of the tachometer-triggered data acquisition. One record has 16 cycles. Noise is measured at 120deg from the rotating axis at distance 0.6m. The rotational speed is 15000rpm for both cases.	P.92
Figure 3.8	Motor noise spectrum.	P.92
Figure 3.9	Spectra of sample data shown in Figure 3.7. The dashed curves are for the raw data and the thick solid curves for the averaged data.	P.93
Figure 4.1	Signals from the striking test using a sampling frequency of 32kHz.	P.93
Figure 4.2	FIR filtering of the signals to exclude the low-frequency drifting and the motor brush induced vibration and noise at the 5 th harmonic of the shaft rotational speed. (a) is the amplitude of the finite impulse response, (b) is the vibration velocity signal with synchronous averaging before filtering, (c) is the vibration velocity in (b) after filtering.	P.94
Figure 4.3	Spectral comparison for (a) the averaged Gutin noise, p_g , (b) the averaged vibration noise, p_v , (c) the casing vibration signal, v_c .	P.94
Figure 4.4	Normalized correlation as a function of the shift index of the signals between sound and vibration. The solid line is for correlation between p_v and v_c , and the dashed line is between p_g and v_c . The maximum correlation (0.924) is found with a shift of 44 data points.	P.95

Figure 4.5	Spectral comparison of a four-blade fan. (a) Raw aerodynamic noise p_1 ; (b) averaged Gutin noise p_g ; (c) averaged vibration noise p_v ; (d) averaged casing vibration v_c .	P.95
Figure 4.6	Analysis of the 2-blade impeller by the one-microphone method.	P.96
Figure 4.7	The correlation indices of the Gutin and vibrational noise with the accelerometer signal for the 2-blade impeller.	P.96
Figure 4.8	The signals from the 4-blade impeller analysed by the one-microphone method.	P.97
Figure 4.9	The correlation indices of Gutin and vibrational noise with the accelerometer signal for the 4-blade impeller.	P.97
Figure 4.10	The study of the cubic power law for the vibrational noise radiation.	P.98
Figure 4.11	The comparison of Gutin and vibration noise for the 2-blade impeller. Legends: p_g means Gutin noise pressure, p_v means vibrational noise, f means that the brush noise at 5rps is filtered, d600 means measured at a distance of $R=600\text{mm}$.	P.98
Figure 4.12	The comparison of Gutin and vibration noise for the 4-blade impeller.	P.99
Figure 5.1	The volumetric flow rate for different number of guide vanes.	P.99
Figure 5.2	The variation of the near field noise with respect to the number of guide vanes.	P.100
Figure 5.3	The schematic diagram of tip clearance modification by adding paper.	P.100
Figure 5.4	Narrow-band spectral comparison between the original sample and modified impeller with smaller tip clearance.	P.101
Figure 5.5	The design of perforated panel for use inside the fan casing.	P.101
Figure 5.6	The comparison of noise with and without the perforated casing.	P.102
Figure 5.7	One-third octave band comparison of the original fan with two successful measures of modifications.	P.102

Abstract

Ventilation fans are widely used in all kinds of consumer products. Hong Kong has a high capacity of manufacturing such consumer products with many factories in the Pear River Delta region. As the living standard improves, the problem of fan noise emission from these products becomes more urgent than the performance of the ventilation fans. Now there is a need to improve the understanding of fan noise and to offer strategies for reducing such noise. This is the motivation behind the current project.

Fan noise has been studied for over half a century and many mechanisms have been understood. In some cases, they are also satisfactorily quantified. But, to the best of such knowledge, much remains to be investigated, both qualitatively and quantitatively. The problem of noise radiation from large turbomachines in aerospace applications has received a lot of attention for obvious reasons. The same is not true for small ventilation fans. Noise from small fans shares many features with that of large turbomachines, but there are important differences. For instance, a turbo-fan aircraft engine may have a diameter of nearly 1m and the gap between the rotating blades and the stationary casing, i.e. the tip clearance, is about 1mm. The flow in this gap is believed to cause a lot of energy loss as well as noise. A much smaller consumer product fan normally has a tip clearance of 2mm. The problem of noise radiation from this region becomes much more severe. The big clearance is required for safety reasons. The issue of safety comes up for consumer products instead of the aircraft because of the low accuracy, hence low cost, at which such fans are manufactured. Because of the

need to keep the cost low, the motor assembly often vibrates fiercely during rotation. This causes a lot of extra noise. This forms a special class of technical problem which is the focus of this project. Specifically, the project aims to separate the component of noise radiated from the body vibration of the fans, called vibrational noise, from the aerodynamic noise caused by the unsteady flow features. Based on the finding of this noise identification, a technical recommendation will be made to reduce the overall noise. A second objective of the project is to test a few preliminary noise abatement measures for the aerodynamic noise, having identified and excluded the vibrational noise from analysis.

The difference in the directivity of the two types of noise is utilized to achieve the purpose of noise separation. The measurement focuses on the detailed history of sound pressure, $p(t)$. The radiation of aerodynamic noise is assumed to be symmetrical with respect to the rotational axis. For an observer standing in the wake of the air flow, the noise measured at a left-hand side point, $p_{a1}(t)$, should be identical to the noise measured at a mirror point on the right-hand side, $p_{a2}(t)=p_{a1}(t)$. On the other hand, noise radiated by the vibration of the motor assembly and the blades will feature the opposite phase relationship of $p_{v1}(t)=-p_{v2}(t)$. Here subscripts 'a' and 'v' stand for 'aerodynamic' and 'vibrational', respectively. The vibration is assumed to be limited on the rotational plane. The components of aerodynamic noise, p_a , and the vibrational noise, p_v , can thus be identified by the measurements of the total noise at the two sides. If the readings at the two symmetrical points are p_1 and p_2 , then the aerodynamic noise and vibration noise can be separated by $p_a=(p_1+p_2)/2$, $p_v=(p_1-p_2)$. The error of such

noise separation will be attributed to the assumptions on the nature of aerodynamic and vibrational noises. In order to assess the accuracy of these assumptions, an accelerometer is attached to the motor assembly and the vibration signal is used for a correlation study with respect to p_a and p_v . It is found that the correlation with p_v is indeed much higher than that with p_a . During the analysis, it is also found that the friction caused by the five brushes inside the motor is particularly noisy, and the filtering of this signal from p_1 and p_2 improves the contrast of the noise correlation.

Attempts are also made to reduce the aerodynamic noise and the total noise. First, the tip clearance is reduced from 2-3mm to 1-2mm by using a flexible membrane which can be regarded as safe for the consumer products. The result shows significant improvement for the air flow capacity under the same rotational speed. The rotational speed can thus be reduced to achieve the same ventilation performance, and the noise is reduced by several decibels. Second, a layer of densely perforated casing is added to absorb the fan noise. The result shows more than 5dB reduction at the peak noise frequency and moderate reduction is also achieved for the overall noise.

Chapter 1: Introduction

Noise is undesirable or unwanted sound. With the advance of scientific understanding of the effects of environment on the inmates of dwellings and factory workers, noise has been identified as an important issue in the design, installation and operation of many machinery. Fans and blowers are among the most common machines that make noise (Leo 1992). The problem of fan noise is not new, but it is becoming increasingly important as consumers demand ever quieter products. Many products mainly consist of fans or use fans, such as hair dryer, hot air brush, computer cooling fans and fan coils used in HVAC systems. This chapter begins with a brief literature survey on the fan noise research, followed by a detailed description of noise mechanisms which are particularly important for small axial flow fans. The directivity of each noise components will be introduced next. The directivity maps will serve as a basis to form the main methodology of fan noise analysis.

1.1 Literature review of fan noise and its control

The acoustic study of rotating machines began with Gutin (1936), whose paper on propeller noise formed a basis for most of the advances made during the next twenty years. He found that the forces exerted by the propeller on the surrounding air generated sound; and the sound was equivalent to an acoustic dipole. Consequently, Gutin studied the following model. Air is subjected to forces distributed over the disk swept out by the propeller; each point on the disk

experiences a constant thrust and drag when a blade passes that point, but no forces at other times. This model essentially yields an analytical solution of the sound produced by a point force, or acoustic dipole, of constant strength rotating in a circle. The sound is composed of a series of discrete tones, whose frequencies are the multiples of the blade passing frequency, $BPF = B \times rpm/60$, where B is the number of blades and rpm stands for revolutions per minute. The sound predicted by this theory was in agreement with the experimental evidence of Gutin's time, both in quality and quantity. But it must be emphasized that this achievement only applied to certain rotating machinery that Gutin encountered, mainly propeller. Propeller noise is dominated by the steady flow mechanisms, and this part of noise is now called Gutin noise. The operation of many modern rotating machinery is by no means steady. The noise spectrum is normally composed of broadband noise distributed over a very wide frequency range, plus a series of superimposed discrete tones at the multiples of BPF. The prediction of the discrete tones is by no means guaranteed when the forces acting on the blades involve complex fluid dynamic phenomena. In fact, the author still has great difficulties in describing some complex flow fields which involve turbulent flow and the interaction of vortices with moving structures. Meanwhile, the prediction of the broadband noise remains a serious challenge even today.

Craik (1985) categorized the fan noise, or turbomachinery noise in general, as interaction noise and self-noise. Here interaction noise means all sounds that result from the encounter of a rotating blade with a time-varying disturbance in a frame of reference moving with the blade element. Self-noise is the sound resulting from flow over the blades themselves and requiring no unsteady inflow.

The two types of noise are often mutually independent, although some changes in viscous flow can be effected by inflow unsteadiness. Gutin noise as described above is a form of self-noise arising from steady flow, and is proportional to the steady loading on the fan blade. This component is generally important at small blade numbers. In terms of the temporal characters, noise can be divided into two types. One is time-locked to the blade rotation, and is called the rotary sound, and the other is not. Longhouse (1976) shows that the rotational noise tends to dominate the measured noise at high flow coefficients when the fan is lightly loaded, and non-rotary noise tends to dominate the noise at low flow coefficients when the fan is heavily loaded. Non-rotary noise mechanisms are random in time sequence. In terms of spectrum, it is broadband with independent peaks occurring in the spectrum.

Apart from the Gutin noise, it is generally accepted in literature that most other noise mechanisms are not fully understood. For example, one of such unexplored mechanisms is the noise caused by the rotor vibration. No systematic study on this topic has been reported in literature. The vibration can be caused either by structural unbalance, hence unbalanced centrifugal forces, or by the unsteady fluid dynamic forces arising from the instability of the fluid flow, or by the limit-cycle flow-induced structural vibrations. In a typical experimental study, such as that by Scharf and Mueller (1995), a four-blade propeller is investigated by both hot-wire and microphone measurements in an anechoic wind tunnel. All noise is normally attributed to the aerodynamic sources. With this background, the following review will focus on the noise caused by the unsteady flow aerodynamics interacting with the smooth rotation of the fan blades.

Noise radiation by the interaction between the rotating blades and the inflow non-uniformity has been widely investigated, both theoretically and experimentally. Trunzo (1981), Scharf (1995), and Majumdar (1998) did some work on the noise of inlet turbulence. Hanson (1974a,1974b) studied the effect of the inlet guide vane wake and the atmospheric turbulence. Mugridge (1975) and Washburn (1988) studied the noise caused by the inlet struts and inlet distortions. The discrete tone radiation is generated through both steady and unsteady blade loading. Steady loading is a function of the pumping requirement, and unsteady loading is generated by spatially periodic inflow distortions. The distortion can be steady in time but vary periodically in space. The latter effect is the dominant generation mechanism for small fans.

Longhouse (1977) showed that, some times, the blade vortex shedding could be a significant source of noise when the fan was operated in a lightly loaded condition. Longhouse (1978) also showed that noise caused by the tip vortex could be dominating, but effective control was achieved by using a rotating shroud to eliminate the usual tip leakage flow. The question then is whether such shroud would tend to induce structural unbalance and hence blade vibration. For an axial flow compressor, the problem of air flow sealing is also transformed from the tip to the upstream and downstream gaps between the rotating shroud and the stationary air flow passage.

Simonich (1993) and Fukano (1986) showed that the unsteady flow caused by the leading-edge vortex and the tip vortex contributed significantly to both broadband and discrete tone noise. Wake flow is also an important area in terms

of noise generated by the unsteady flow features. In a fan stage consisting of a rotor followed by a stator, the rotating wake is probably the most important noise source. Many researchers have tried to optimise the wake arrangement for such fan stage. Waitz (1996) and Rao (2001) carried out experimental investigations aimed at reducing the unsteady stator-rotor interaction using active flow control. The fan rotor was subjected to circumferential periodic distortions. It was shown that the successful re-energizing of the wakes could influence the far-field sound pressure level at the blade passing frequency. Brookfield (2000) proposed a new technique for reducing rotor-wake-stator interaction noise by injecting air from near the trailing edge of the rotating fan blades to fill in the mass/momentum deficit of the rotor wakes. Significant filling of the time-mean wake profile was achieved at 1.5 chord length downstream of the rotor with reductions in the noise amplitudes in the first three BPF of up to 85%. In addition, stator measurements also showed reductions in the stator unsteady loading of up to 10dB. The results demonstrated that the trailing edge blowing was effective for reducing the rotor wakes and their mean harmonic amplitudes. Therefore, with appropriate blade design, significant noise reductions were possible while maintaining rotor-stator spacing. Alternately, the rotor-stator spacing may be significantly reduced while maintaining similar radiated noise levels.

The technique of active noise control has also been investigated. Fitzgerald & Lauchle (1984), and Lauchle et al (1997) focused on the discrete frequency noise reduction in an axial-flow fan by using active noise control technique. The noise at the fundamental BPF was reduced by 20dB at the sensor location, while the second and third harmonics were reduced by 15 and 8dB, respectively. Gerhold

(1997) reported an experiment to control the noise radiated from the inlet of a ducted fan using a time domain active adaptive system. Despite the obvious success, the use of active noise control technique remains expensive and relatively unreliable at present. It is still better to eliminate noise at its source by first seeking a comprehensive understanding of the issue.

So far, the studies on fan noise are almost entirely focused on large-scale turbomachines, many favourable results are relevant to the flow at high Reynolds number. The unsteadiness is usually characterized by large scale in time and spatial domains. Very limited amount of work has been conducted for the systematic understanding of the noise generation mechanism for small axial flow fans. In terms of noise abatement, some previous experiments have demonstrated that the noise reduction may be initially achieved by correcting a grossly incorrect flow condition, but further improvement and optimisation are rather difficult due to the complicated nature of fan aero-acoustics.

For small axial flow fans, noise radiation is becoming an important issue for both manufacturers and the consumers. Due to the limitation of diameter, it takes much higher rotational speed to achieve the same tip speed, hence a given volume flow rate. Such high rotational speed gives rise to high noise partly because of the vibration experienced by the rotors. The vibration can be easily caused by the unbalance of the rotor when it is first manufactured, or the natural wear during the life span of the product. The issue of identification of the exact noise source becomes complicated and yet important. Without a methodology of source identification for vibrational and aerodynamic noises, it is impossible to

recommend a strategy for improvement. Since there has not been any literature on this topic, the author wishes to fill this gap.

1.2 Fan noise mechanisms

Different fans have different acoustic characteristics, but they share similar noise mechanisms. In general, fan noise can be divided into three groups:

- (1) Noise is radiated by the structural vibrations such as the motor-fan assembly or other parts of the product due to the unbalanced operation.
- (2) Noise is radiated by the steady operation of the fan. This part of noise is known as the Gutin noise as Gutin (1936) made much contribution towards the subject. More description will be given shortly.
- (3) Noise is also made by the unsteady operation of the fan relative to the rotating reference frame. There are many factors that will give rise to this noise. In many practical applications, this mechanism is believed to be dominant over the Gutin noise.

1.2.1 Vibrational noise

Machine vibration is mainly caused by the unbalance of rotating parts. This could be caused by the poor manufacturing quality, or by the natural wear during the life of the product. The problem of poor balance is particularly serious for low-cost consumer products, such as hair dryers, since there is a lack of

expensive quality control for each piece produced. On the other hand, hi-tech products like aircraft compressors are well balanced and the noise made by this mechanism is negligible compared with noise from other sources. It will be shown later that, for the demonstration, the vibrational noise is as important or even more important than other components of noise. Significant sources of vibration are listed as follows:

- (a) unbalanced motor operation,
- (b) unbalance of the fan blades,
- (c) poor installation of fan blades onto the motor axis, and
- (d) brushes inside the motor.

(d) can be rather important. The brushes have constant friction between the moving and stationary parts. This friction generates noise, which has a frequency equal to the number of brushes times the rotational speed. This noise is found to be very dominant in some examples to be shown later. Motors without brushes are normally not as powerful and not as widely used in consumer products. Even for brushless motor design, the bearing will still make some noise. The purpose of this project is not to reduce vibration noise through structural improvement, but rather to exclude this noise components based on the spectral characteristics of this noise(Yahya 1983).

1.2.2 Gutin noise

A fan blade is simply a rotating wing, subject to the same forces as conventional wings: lift and drag. Frictional drag is unimportant in this case. The lift force on

a blade is projected onto two directions. One is parallel with the inlet flow, and the component is called thrust. Another is the circumferential direction which is against the rotation, and it is therefore called a drag. This drag is responsible for the torque required to drive the fan, so that the noise associated with this force component is also called torque noise. Both thrust and drag do not generate noise if they are steady relative to the observer. But the observer in question now stands on the ground, while the fan blades rotate. To this observer, the steady rotation of fan blades represents a periodically unsteady pattern of flow field. Noise is made by this unsteady pattern. The noise made by the two forces discussed above is collectively called the loading noise. In addition, the blade pushes air around, and this event creates a noise very much like that from a loudspeaker diaphragm. When the front of the blade is pushing the air causing compression, the opposite side of the blade causes expansion or rarefaction. If the blade thickness vanishes, the noise made by the two surfaces cancels each other out. As all blades have a finite thickness, the cancellation is normally incomplete. The residual noise is called the thickness noise. Gutter noise includes both thickness noise and loading noise when the rotation of the fan blade is running at absolutely constant speed.

1.2.3 Unsteady flow noise

Noise is generated by the unsteady pressure on structural surface. There are many situations where unsteady flow is created.

First, the inlet flow to a blade can be unsteady due to turbulent eddies from protection grid. Sometimes, the struts are located at upstream positions. Then they will cause an inflow with regular vortices shed from the struts. The length scale of these vortices can be small relative to a blade chord (such as introduced by flow over a heat exchanger or in a duct boundary layer). The noise produced is a function of the turbulence intensity, the length scale of the turbulence, and the lift of the blade. Since turbulence is generally broadband in frequency content, these forces map through to a broadband noise spectrum. The inflow disturbances cause a local change in blade angle of attack. The change of the angle of attack causes a change in the lift on the blade. Since these disturbances appear periodically to a rotating blade, they cause pure tones. These pure tones obey a certain power law with respect to the blade rotational velocity. Disturbances can be located either upstream or downstream, although upstream disturbances are typically the worst offenders.

Second, unsteady flow can come from a steady inflow but with a wrong direction. The incident angle can be too large for flow to turn around the blade surface. As a result, flow separation occurs. A separated flow is always unsteady.

Third, turbulent flow on the blade surface can cause noise. Turbulent flow is found whenever the Reynolds number is large enough. Within the turbulent boundary layer, the flow is unsteady but the energy of such flow oscillation is confined locally. This unsteady flow kinetic energy convects with the free stream velocity along the surface until the process is disrupted by the trailing edge. At the trailing edge, part of the convected oscillation energy is transferred to sound and the sound appears to be generated at the trailing edge. This noise is called the trailing edge noise. It is also possible that flow near the trailing edge can cause vortex shedding there. For example, when the trailing edge is very bluff. Stall noise is an extreme case of trailing edge noise. Again, the spectrum produced is broadband in nature, and related to the characteristics of the blade boundary layer and the trailing edge.

Last, but certainly not the least, the tip clearance of blades installed inside a casing. With the absence of aerofoil structure in the gap, the pressure difference built up at lower radial positions causes a leakage flow over the tip. The flow appears to be a shear layer which rolls up as a tip vortex. This vortex causes noise both by its interaction with the trailing edge and, under high fan loading, with the leading edge of the next blade. It is often an important noise source.

In order to operate a fan with low noise, it is important to do so at a condition where the fan has its maximum efficiency. Low rotational speed and low pressure difference between upstream and downstream of a fan will also reduce noise. It is also critical to avoid using structures that cause non-uniformity of flow in ducts. The use of flexible fan mounting can reduce vibration induced

noise. The use of sound absorbing walls can also contribute to the noise abatement.

1.3 Directivity of isolated impeller noise

Directivity refers to the distribution of sound power as a function of the direction of the source-observer vector in relation to certain source orientation. Each component of noise source has its own directivity, and this is the basis for this project to separate noises from different sources. The directivity of the aerodynamic noise is well known, although a collection of all components is rather hard to find in open literature. The directivity of the vibrational noise is the result of the author's study. Before the introduction of these maps, it is perhaps informative to start with the elementary sound sources.

At the most elementary level, all the noise sources can be classified as monopole, dipole or quadrupole. A monopole is like a pulsating sphere. The sphere expands and contracts at a uniform rate in all directions. The noise created by this source is also uniform in every direction. As shown in Figure 1.1, when two monopoles of opposite phase (180° different) are put together, most of the sound radiated by the two sources cancel each other out. The amount of sound left depends on the proximity of the two sources as well as the strength of each source. If the two sources approach each other in a way that keeps the product of the strength and distance constant, there is always a certain amount of residual sound. The extreme case of zero distance and infinite strength for each monopole represents the ideal

source called a dipole. Similarly, two dipoles can be arranged to form a more complicated elementary source called quadrupole.

Noise radiated by the blade thickness is described earlier. The front of the blade compresses air and can be described as a positive monopole. The back is a negative monopole. The two are equal in strength and opposite in phase, exactly like the concept of a dipole formed by two monopoles. Unlike the conceptual dipole described earlier, the two monopoles from a fan blade do not approach each other indefinitely. But since their distance (thickness) is so small compared with the wavelength, it is much better to regard the thickness noise as a dipole located at the center of the two surfaces than referring it as a distribution of monopoles. The latter is frequently done in literature and it can prove to be misleading. The important point is that the sound radiated by the thickness noise should have a dipole character instead of a monopole. For a dipole, there is no sound radiation in the axis perpendicular to the axis of the dipole, which can be a point force or the line linking the positive and negative monopoles. This argument leads to the conclusion that there is no thickness noise on the rotational axis of the fan since it is perpendicular to the rotational velocity. The directivity of the thickness noise is shown in Figure 1.2. The '+' labels refer to the phase angle, which in this case is uniform for all directions. Such uniform phase distribution is caused by the angular symmetry of the blade rotation.

The loading on each blade is divided into thrust and drag, as shown in Figure 1.3(a). The directivities of the thrust and the torque noises are shown in Figures 1.3(b) and 1.3(c), respectively. The thrust noise has opposite phase across the

rotational plane since the thrust has fixed direction. The noise on the rotational plane vanishes because of the different directions in which the thrust forces are being rotated on different blades. The result is a directivity with two null axes instead of one for a point dipole. The torque noise is like the thickness noise since they have almost identical topological distribution. Figure 1.3(d) combines the thrust and the torque noise as the total noise from the steady loading. The noise downstream of the rotational plane is stronger than upstream due to the different interference patterns between the two components of loading forces.

In this project, it was suspected a strong tendency for the motor-fan assembly to vibrate due to many reasons outlined earlier. The vibrations can be divided into axial movement, rotational vibration as well as bending and distortion of the blades. It was assumed that the rotational motion of a rigid-body, as illustrated in Figure 1.4(a), is dominant. Under this assumption, the noise directivity should be the same as the one shown in textbooks for an oscillating cylinder. The rigid body assumption is not fully tested in the experiment, but the resultant noise directivity is. The noise directivity is shown in Figure 1.4(b). The anti-phase relationship for the two sides of the rotational axis is unique among all directivity maps shown so far. In other words, if one subtracts the noise measured at a location in the northern hemisphere, p_1 , by the noise measured at the mirror position in the southern hemisphere, p_2 , the component of noise radiated by the vibration is doubled while that by the Gutin noise (including both loading and thickness noises) will cancel out. Vibrational noise and Gutin noise can be recovered by the difference and summation of the two measurements as follows:

$$p_v = \frac{p_1 - p_2}{2}, \quad p_g = \frac{p_1 + p_2}{2}. \quad (1.1)$$

Noise radiated by unsteady flow conditions is difficult to specify. If the unsteadiness is time-locked with the blade rotation, it may have a fixed directivity pattern which may or may not have a symmetrical pattern. If the unsteady flow is random, it can be filtered out by the synchronous averaging technique to be described a little later.

1.4 Objectives and methodology of this project

Manufacturers of consumer products are making efforts to reduce the noise emission of their products and labels like 'quiet' or 'silent' have become a crucial sales gimmick. Typical examples are seen in 'silent' hair dryers, 'quiet' window-type air conditioners, etc. It is essential to identify the exact source of noise before any contribution can be made to improve such products. The main objective in this project is to distinguish the contributions of the two types of noise: aerodynamic noise and vibrational noise. If the aerodynamic noise is dominant, then it makes sense to work on the improvement of aerodynamic design of the fan blades. Otherwise, the manufacturers are simply advised to produce fans with better structural quality and use better motor in order to avoid vibrations. Of course, the cost will then go up. But it will be worthwhile if the noise will be reduced. The scenario of flow-induced vibration, which involves both blade aerodynamic redesign and structural improvement, will be left to future studies.

To start with, a fan from a hair dryer was taken as the working sample. The principle established will be directly applicable to other types of fans such as the

electronic cooling fans and other ventilation fans. Hair dryer is a common product in the market. Statistics show that Hong Kong produces nearly 12 million hair dryers a year. As shown in Figure 1.5(a), it contains a DC motor, a fan impeller, downstream guide-vanes (not shown clearly), casing and heating elements. In the experiments, the heating element is removed in order to simplify the study. Shown in Figure 1.5(b) is the photograph of the impeller mounted on a cylinder which houses the motor assembly. The impeller is isolated again for the purpose to understand the elementary noise source better. Some measures to reduce the noise of the whole set of hair dryer will be described in Chapter 5. Before that, most studies are conducted for the isolated impeller shown in Figure 1.5(b) with or without a short cylindrical casing around the impeller. The most common rotational speed is 15000 rpm, which makes a BPF of 1kHz for an impeller of four blades. The blades are like elephant ears, which features a serious leading edge sweep with blade width increasing drastically from the hub to the tip. The blades are so wide at the tip that they are almost equivalent to eight or more narrow blades. It is possible that the noise radiated by each blade at different radius may interfere destructively. In other words, the impeller may well be a 'quiet' design. It would be interesting to compare the noise from this impeller with others having the same aerodynamic performance. But this is also left to future studies.

The main methodology and plan of the project are outlined here.

- (1) The flow field will be analysed as thoroughly as our equipment allows, and a conclusion will be drawn about whether the fan is working in a

satisfactory state. If this is not the case, one would suspect a huge turbulent flow noise, and this impeller will be regarded as being not worthwhile for the further acoustic effort. The conclusion from this analysis is that the fan is working reasonably smoothly in terms of aerodynamics.

- (2) Measurements will be conducted to get the time-domain sound pressure using multiple sensors including a tachometer for the purpose of data averaging and the filtering of the non-rotary sound. The contributions from the vibrational and aerodynamic noises will be analysed according to the summation-subtraction formulas of equation (1.1). If the vibrational noise is found to be dominant, it is sensible to proceed with measures of vibration reduction. But this is beyond the time scope available to this project. The emphasis is on the following step.
- (3) A coherence study between the vibration measurement with the aerodynamic noise p_g and vibrational noise p_v will be conducted. The result validates the hypothesis about the nature of vibrational noise.
- (4) Several attempts will be made to reduce the aerodynamic noise of the fan.

Chapter 2: Flow measurement and analysis

For most air-flow measurements, engineers cannot use direct methods, but have to resort to the measurement of some physical effect arising from the motion. Three such effects have been found by experience to be suitable; pressure changes associated with the motion (Bernoulli effect); consequent mechanical effects, such as the rate of rotation induced in a rotor made up of light vanes mounted in the stream; and the rate of cooling of a hot body, such as electrically heated wires, introduced into the air current. Of these, the first is most important and most straight forward. This is realized by the so-called Pitot-static tube. When such a tube is suitably inserted in the stream, it records a pressure difference from which the flow velocity is derived by the Bernoulli equation. It may be used without calibration as a standard for the measurement of air speed. This is not true of anemometers which depend on either mechanical or electrical effects. Such instruments are subject to individual variations which is difficult to control, and usually require calibration against a standard instrument of the pressure-measuring type.

In this chapter, the flow will be measured firstly by a Pitot-static tube. The volume flow rate will be calculated and the velocity triangle analysis will be conducted to see whether the flow over the aerofoil is well behaved. Then hot-wire velocity anemometer is used to see more details of the wake flow. The purpose is to see whether a clear wake structure can be identified and this information will help understand the results of noise measurement.

2.1 Velocity measurement by Pitot-static tube

A Pitot-static tube measures the pressure difference between the static pressure and the total pressure. The structure of the device is shown in Figure 2.1(a). The measurement of the total pressure is achieved by providing an orifice at the head and by connecting it to a manometer. There is abundant experimental evidence to confirm that the pressure indicated by a properly aligned open-ended tube facing the current is not too sensitive to the alignment. The head of the tube is bent at right angles to the stem and its walls are parallel to the direction of flow. Such head deflects the air only slightly, and at a short distance back from the tapered portion a number of small holes are drilled. The other end of the stem is connected to another manometer. The difference between the stagnation pressure and the static pressure is read from the two inclined-tube manometers and the difference is equated to the dynamic head of incompressible flow, $\frac{1}{2}\rho_0 V^2$ where ρ_0 is the air density and V is the local flow velocity which must be parallel to the tube. The advantages of using Pitot tube are that it is a simple, inexpensive and durable instrument. Moreover, an inexperienced operator can obtain moderate accuracy from it. The disadvantage of using Pitot tube, like all differential-pressure flow meters, is that it has a square root characteristic.

Figure 2.1(b) shows the measurement points inside the circular duct which houses the fan impeller. The Pitot tube needs to be located in a clear, straight duct section providing at least 8 diameters upstream and 2 diameters downstream of the Pitot tube free of the elbows, transitions, or reductions. In this case, the inlet section of the whole hair dryer fan is put inside a duct of 10cm in diameter.

The inlet flow is measured according to positions shown in Figure 2.1(b). The resultant flow velocity is integrated to find the volume flow rate. The result for 15000rpm is $36 \times 10^{-3} \text{ m}^3/\text{s}$, which is close to the product specification. Note that this value is measured with the complete hair dryer and with heating elements intact. The value of the volumetric flow rate would be a lot higher when the impeller is tested in isolation.

2.2 Velocity triangle analysis

It is customary to analyse the flow through turbomachines in a reference frame that rotates with the impeller. This is called the relative reference frame. The velocity measured on the stationary ground is called the absolute velocity, while the velocity seen in the relative reference frame is called the relative velocity. Mathematically, the relationship can be expressed as $\vec{V}_{abs} = \vec{u} + \vec{V}_{rel}$, where the three vectors are, respectively, the absolute velocity, the rotational velocity, and the relative flow velocity. The triangle is shown in Figure 2.2. The relationship forms a triangle and the analysis is called the velocity triangle analysis in the design of turbomachines. Notice that the blade is rather three-dimensional in nature, but an initial analysis at the average radius will still provide important information as to how the impeller behaves at a certain rotational speed.

The radius at the hub and tip are 13.5mm and 29.8mm, respectively. The casing has a radius of 31mm. Due to the special shape of the blade, the analysis of the

flow at a mean radius of 25mm is chosen, the inlet velocity is found by dividing the volumetric flow rate by the passage area,

$$V_1 = \frac{Q}{\pi(r_{up}^2 - r_{hub}^2)} = \frac{36 \times 10^{-3} \text{ m}^3 \text{ s}^{-1}}{\pi(0.0298^2 - 0.0135^2) \text{ m}^2} = 16.2 \text{ m/s}. \quad (2.1)$$

The rotational speed at the mean radius is

$$u = \omega r = 2\pi \times \frac{15000}{60\text{s}} \times 25 \times 10^{-3} \text{ m} = 39.1 \text{ m/s}. \quad (2.2)$$

The relative velocity (V_{r1}) of the fluid with respect to the impeller blade is formed by

$$V_{r1} = (\sqrt{u^2 + V_1^2}) \text{ m/s} = (\sqrt{39.1^2 + 16.2^2}) = 42.3 \text{ m/s}. \quad (2.3)$$

The relative flow angle at inlet is found to be

$$\beta_1 = \tan^{-1}\left(\frac{V_1}{u}\right) = \tan^{-1}\left(\frac{16.2}{39.1}\right) = 22.5^\circ. \quad (2.4)$$

For the inlet blade angle is measured to be $\beta_{1s} = 35.5^\circ$, the angle of attack, or incidence angle is found to be

$$\alpha_{in} = \beta_{1s} - \beta_1 = 35.5^\circ - 22.5^\circ = 13^\circ. \quad (2.5)$$

The exit flow can only be analysed if one knows the deviation angle, which is defined as the difference between the blade exit angle and the actual flow angle,

$$\delta = \beta_{2s} - \beta_2. \quad (2.6)$$

This information is not normally available, but a value of 5° can be adopted based on empirical data accumulated in this field of study. This gives the exit flow a direction of $\beta_2 = \beta_{2s} - \delta = 35.5^\circ - 5^\circ = 30.5^\circ$ as the blade itself is nearly a flat plate rounded off at the leading and trailing edges. For axial flow fans with almost constant passage area, the axial flow velocity at the exit is equal to that at

the inlet, V_1 , due to mass conservation. The difference between the rotational speed u and the circumferential component of the relative exit flow is

$$V_{w2} = \frac{V_1}{\tan \beta_2} = \frac{16.2}{\tan(30.1^\circ)} = 27.5 \text{ m/s}. \quad (2.7)$$

The exit flow angle is found as

$$\alpha_2 = \tan^{-1} \left(\frac{V_1}{u - V_{w2}} \right) = \tan^{-1} \left(\frac{16.2}{39.1 - 27.5} \right) = 54.4^\circ. \quad (2.8)$$

By the measurement of the downstream guide vane, the angles at hub and tip are 62.7° and 67° respectively. The value at the mean radius is around 65° . That gives the incidence angle for the guide vane as,

$$\alpha_{gv} = \alpha_{2s} - \alpha_2 = 65^\circ - 54.4^\circ = 10.6^\circ, \quad (2.9)$$

which is coincidentally quite close to the incidence angle for the impeller.

Both incidence angles are a little high and, judging from the blade shape, a considerable amount of turbulent flow will be generated leading to broadband noise. Having said that, the blade geometry is not grossly wrong for the fan to work at this rotational speed. More accurate assessment of the flow field quality is provided below by the hot-wire measurement.

Before the introduction of the hot-wire measurement, it is useful to estimate the Reynolds number based on the fan camber of about 2.5cm:

$$\text{Re}_l = Ul/\nu = 15 \times 0.025 / (15 \times 10^{-6}) = 25 \times 10^3, \quad (2.10)$$

where U is the average velocity, l is the length of duct, and ν is the kinematic viscosity.

It is well known that for an ideal flow over a flat plate with zero incidence angle, turbulence occurs around a Reynolds number of 200×10^3 . Similar critical Reynolds number exists for flow through a bluff body like a cylinder based on its diameter. It is therefore possible that the flow in this case can be laminar in general, but organized vortex shedding may occur due to the high incidence angle, making the flow effectively turbulent.

2.3 Hot wire measurement

Thermal anemometers measure fluid velocity by sensing the changes in heat transfer from a small, electrically heated sensor exposed to the fluid motion. They are generally small in size and have good frequency response. It makes them especially suitable for studying flow details, particularly in turbulent flow. Flow through the fan is likely to be turbulent in general due to the complex geometry.

To measure velocity details in a flowing fluid, the ideal instrument should have high-frequency response to accurately follow transients; be small in size for an essentially point measurement; measure a wide velocity range; measure only velocity, and work in a wide range of temperature, density, and composition, measure velocity components and detect flow reversal; have high accuracy; have high resolution; create minimal flow disturbance. For many years, only the hot-wire anemometer satisfied enough criteria to be used extensively in turbulence studies. Pitot probes, flow visualization, and other techniques complemented hot-wire data but generally could not provide details as well as hot wire.

The flow field through the fan is absolutely unsteady when viewed from the stationary observer. This is explained in the last chapter for the Gutin noise. If the fan is designed perfectly, the flow field could be steady when viewed in the relative reference frame. In most cases, even flow in the relative reference frame is unsteady. The extent to which the flow is unsteady in the relative reference frame is one of the main interests in the measurement using hot-wire. Ideally, the instrument can be mounted to the rotating blade and the reading gives the value of flow through a point fixed in the relative reference frame. But this requires very miniature sensors to be burried inside the fan blades and there is special requirement for the contact between the rotating cables carrying the signal and the fixed instrument to read the signal. Such instrument is available but rather expensive. They are normally used in aerospace applications. In any case, the fan blade is too small to mount any miniature sensors currently available in the market. So, the only option left is using hot-wire sensors fixed on the ground. What the sensor measures is the flow velocity for different points in the relative reference frame, say P , passing through the fixed sensor position, say P_{abs} . Assuming that P is located at the cylindrical coordinate of (r, Φ_0) in the relative reference frame, the angular position of P_{abs} in the absolute reference frame is

$$\Phi_{abs} = \Phi_0 + \omega t . \quad (2.11)$$

If the data acquisition is done at a rate of F_{abs} points per second, the time interval between two data points is $1/F_{abs}$, which means an angular resolution of

$$\Delta t = 1 / F_{abs}, \Delta \Phi = \omega \Delta t . \quad (2.12)$$

The data record for a variable U becomes
 $U(\Phi_0, t), U(\Phi_0 + \Delta \Phi, t + \Delta t), \dots, U(\Phi_0 + 2\pi, t + T), U(\Phi_0 + \Delta \Phi, t + T + \Delta t), \dots,$

where $T = 1/\text{rps}$ is the period of rotation. For every blade rotational cycle, one reading for velocity at P is taken. The space resolution is $\Delta\Phi$. For the present experiment, it has $F_{abs}=20\text{kHz}$, and $\text{rpm}=15000$. So that the angular resolution and the real sampling frequency(F_s) in the relative reference frame are

$$\Delta\Phi = 2\pi \times \left(\frac{15000}{60} \right) / 20 \times 10^3 = 4.5^\circ, F_s = 15000 / 60 = 250\text{Hz}, \text{ respectively.}$$

The mechanism of the hot-wire manometer is described as follows. When an electric current goes through the sensor, the sensor will be heated. The heat-generation rate by the electrical current I is

$$Q_g = I^2 R_w, \quad (2.13)$$

where R_w is the sensor resistance. By ignoring the heat storage, there is a balance between the heat transfer from the hot-wire to the ambient air, Q_t , and Q_g , i.e.

$Q_g = Q_t$. Q_t is a function of flow velocity U , wire temperature T_w , ambient temperature T_a and so on: $Q_t = f'(U, T_w, T_a \dots)$.

Thus the flow velocity can be determined as

$$U = f(I, R_w, T_w, T_a \dots). \quad (2.14)$$

There are two main modes of operating a hot-wire probe: (a) the Constant-Temperature (CT) mode, in which the probe resistance (and thereby its temperature) is kept virtually constant by varying the current; (b) the Constant-Current (CC) mode, in which the probe temperature varies. The CT anemometer is much simpler to use than the CC type, and has a higher frequency response, so most velocity measurements are now carried out with CT mode.

Since the flow through a fan is three-dimensional in nature, it is required to measure many components of velocity. It is difficult to measure all components at the same time. It is tentatively assumed that the flow in the radial direction is much smaller than those in the axial and circumferential directions. This condition can be satisfied if the impeller is confined inside a cylindrical casing where the radial velocity is definitely zero. An X-wire is chosen to measure two velocity components of a two-dimensional flow field simultaneously.

Figure 2.3 illustrates a typical X-wire probe and the principle of an X hot-wire. The two wires formed a plane. Provided that the velocity component perpendicular to the X-probe is small compared with the two in-plane components U and V , the simultaneous response for the two wires can be expressed as

$$E_1 = F_1(U, V), E_2 = F_2(U, V). \quad (2.15)$$

When the angle θ is in the range of $-45^\circ \sim 45^\circ$, there is a unique relationship between (E_1, E_2) and (U, V) . U and V can be determined from the response of the two wires for both steady and unsteady flow analysis.

In the present experiment, tungsten wires, $5\mu\text{m}$ in diameter and with an active length of about 2mm , were used with constant temperature circuits. In this case, the frequency response is greater than 20kHz , which are sufficient for the present measurement of steady flow velocity, but perhaps insufficient for unsteady flow measurement for the relative reference frame. The cut off frequency was set at 9.2kHz . The duration of each record was about 10sec .

The X-wire probe was calibrated and the process is described here. The signal analysis is usually carried out in terms of the effective velocities, V_{e1} and V_{e2} , for the two wires. If the definition of the magnitude of velocity vector \vec{V} as \tilde{V} , then

$$V_{e1} \cos \alpha_1 = \tilde{V} \cos(\alpha_1 + \theta), \quad V_{e2} \cos \alpha_2 = \tilde{V} \cos(\alpha_2 - \theta). \quad (2.16)$$

Then it has

$$\theta = \tan^{-1} \left(\frac{V_{e2} - V_{e1}}{V_{e1} \tan \alpha_2 + V_{e2} \tan \alpha_1} \right), \quad (2.17)$$

and

$$\tilde{V} = V_{e1} \frac{\cos \alpha_1}{\cos(\alpha_1 + \theta)} = V_{e2} \frac{\cos \alpha_2}{\cos(\alpha_2 - \theta)}, \quad U = \tilde{V} \cos \theta, \quad V = \tilde{V} \sin \theta. \quad (2.18)$$

In the calibration process, α_1, α_2 (cf. Figure 2.3) should be measured, and the relationship between the effective velocity V_{e1}, V_{e2} and the wires response E_1, E_2 should be determined. Usually, V_{e1}, V_{e2} can be expressed as polynomial functions of E_1, E_2 , respectively, and a third order polynomial fit is sufficient, i.e.

$$V_{e1} = C_{1,0} + C_{1,1}E_1 + C_{1,2}E_1^2 + C_{1,3}E_1^3, \quad (2.19)$$

$$V_{e2} = C_{2,0} + C_{2,1}E_2 + C_{2,2}E_2^2 + C_{2,3}E_2^3. \quad (2.20)$$

The calibration was carried out in a wind tunnel, which gave the above polynomial coefficients.

Figure 2.4 presents the measurement method schematically. The four-blade fan impeller was used in the experiment. The fan and the casing were positioned carefully, so that the gap between them, or the tip clearance, was uniform around the circle. The two ends of the casing were smoothed by a bellmouth so as to reduce the boundary layer thickness and turbulent intensity of the inlet flow. The

fan was driven by a DC motor, which can be made to run at different rotating speeds by adjusting the input voltage.

In order to get a valid reading from the X-wire, the flow direction should be aligned with the probe axis as much as possible. Based on the earlier velocity triangle analysis, the velocity vector at the outlet of the fan deviates from the fan axis was known, so the hot-wire probe axis was inclined 20° to reduce the measurement error. The X-wire probe was located at 2mm behind the exit of the blade row. It traversed from the hub to the tip of the blades to measure velocity components at the radial positions of $r=16.5, 17.5, \dots, 29.5$ mm. Due to the spatial limitation, points very near to the hub and the inner casing wall cannot be measured. The values at these points can only be obtained through extrapolation. Measurements were made for three typical rotation speeds, 10000, 12000 and 15000 rpm.

2.4 Flow field analysis

By averaging the values at each radial position, the circular average velocity, $\bar{U}(r), \bar{V}(r)$ are obtained, and the results are shown in Figure 2.5 for over 500 rotational cycles. The maximum flow velocity occurs at approximately 3mm down from the tip. The flow around the tip has low speed due to the leakage. When the tip clearance is increased from 1mm to 2mm, the tip leakage increases and the radial position of peak flow velocity shifts inwards.

The axial velocity is used to get the volumetric flow rate by integration from the hub to tip, as well as the average axial flow velocity U_{av} ,

$$Q = \int_{r_{hub}=15mm}^{r_{outer}=32mm} 2\pi r \bar{U}(r) dr, U_{av} = Q / \left[\pi (r_{outer}^2 - r_{hub}^2) \right]. \quad (2.21)$$

The result is given in the following table.

Table 2.1 The volume flow rate measured by the hot-wire anemometer for 2mm tip clearance

Rotating speed (rpm)	Volumetric flow rate (m ³ /s)	Average axial velocity (m/s)
10000	0.030	12.0
12000	0.036	14.3
15000	0.045	17.9

The volume flow rate for 15000rpm is 0.045m³/s, while that measured by the Pitot-static tube was 0.036m³/s. The difference is around 25%. Apart from some measurement error, the main reason for this discrepancy is the difference in configuration. In the Pitot-static tube measurement, the impeller was installed in the hair dryer and the hair dryer was inserted in a large tube for the measurement. In the hot-wire measurement, the impeller is isolated and there is no resistance to air flow by any obstacle.

If the velocity triangle analysis for the average radius of the isolated impeller is conducted again, the incidence angle can be found as follows with the help of Figure 2.2,

$$\alpha_{in} = \beta_{1s} - \beta_1 = 35.5^\circ - \tan^{-1}(17.9/39.1) = 10.9^\circ.$$

The incidence angle is relieved by a few degrees compared with the rotation of the impeller inside the hair dryer.

If the velocity values are averaged for each observation point P fixed to the relative reference frame, then a distribution of local average velocity as a function of the angular position Φ_0 will be obtained. The difference between the average and the instantaneous values becomes the function of rotational cycles. The standard deviation of local velocity is plotted together with the local average velocity in the format of vertical bars in Figure 2.6 for the axial velocity component U and in Figure 2.7 for the circumferential velocity component V . First of all, the curves have four valleys representing the four blade positions. The standard deviation is small in both hub and tip positions. The maximum oscillation is seen around the radius of 26mm. This was perhaps the location where the tip vortex hit the blade. This should also be the position where the unsteady flow noise source is concentrated. The ratio of oscillating velocity to the mean velocity is approximately 1/3 at this position.

In conclusion, the flow through the fan blades has around 10° of incidence angle. Judging from this angle and the detailed geometry of the leading edge, it is likely that the flow is separated near the leading edge. The hot-wire measurement at the exit of the impeller basically confirms the finding of the Pitot-static tube, and it gives useful information about the unsteady flow pattern in the relative reference frame. The most unsteady flow occurs around $r=26\text{mm}$ and the ratio of the velocity oscillation to the mean velocity is as high as 1/3. It is likely that the noise generated by the unsteady flow may be very important.

Chapter 3: Noise and vibration measurement

In order to find noise directivity for the fan, sound pressure values at different observer points need to be combined linearly in different ways. For example, the vibrational noise felt at the two sides of the rotational axis has opposite phase, while the Gutin noise has the same phase, cf. Figures 1.3 and 1.4. Therefore, by subtracting noise measured at one point by its mirror point on the other side will eliminate the component of Gutin noise c.f. equation (1.1). This process requires that the two microphones have identical response to sound. Theoretically, there is no pair of identical microphones in the world. It is always necessary to calibrate one microphone against the other in terms of both amplitude and phase angle. This is routinely done in sound intensity measurement. The author therefore set out to learn this technique by participating in a duct acoustics project in which accurate calibration of microphones were very crucial. The author made a significant contribution to that project in terms of the measurement work using chirp sound source. The work was published in 2000 (Huang et al 2000). The measurement focused on the speed of sound propagating in a duct in which one wall was a tensioned membrane. The purpose of adding the membrane was to influence the acoustic properties of the duct. The potential application of the study is noise control in the duct. The project is only briefly described in the next section, followed by the use of calibrated microphones in the complete set-up of the fan noise and vibration measurement.

3.1 Calibration of two microphones

Sound waves are reflected by all solid structures, and the reflected sound interferes with the incident sound to form complicated standing waves. Standing waves in a duct is the simplest case. In order to find out how much sound is propagating in each direction, it needs at least two microphones, just as two equations are needed to solve for two unknowns. The two unknowns in this case are the amplitudes of the incident and reflected waves. If the two microphones are identical, measurements by the two microphones can help finding the two amplitudes. On the other hand, if the microphones are not identical, but the two amplitudes are known to obey a certain relationship, the same principle can be used to calibrate the response of the two microphones. The simplest way to do so will be to install the two microphones at two points where the sound waves are known to be exactly equal. This can be created by having two microphones inserted at the two opposite sides of a duct in which sound waves are propagating. As far as the waves are of low frequency and thus have plane wave front, the sound pressure should be constant over the entire cross section. Plane wave can be achieved by keeping the frequency below the cut-on frequency of the duct, which is $c/2h$, where c is the speed of sound and h is the duct height. It is pointed out that, due to practical limitations, the sound pressure at any two points are never exactly identical. Furthermore, the sound pressure readings of microphones also depend on the method to insert the microphone in a duct. It is therefore not guaranteed whether the calibrated microphones can be trusted when they are used in different circumstances. The most straight forward method is to calibrate the two microphones at the positions where they will be used. Since

now the readings at the two positions are different, it will be necessary to swap the microphone to get another set of data. The calibration method is illustrated in Figure 3.1.

For sound with a single frequency, which can be generated by driving a loudspeaker with a function generator, the acoustic pressure and its amplitude inside the duct with standing waves can be written as

$$p = Ae^{i(\omega t - kx)} + Be^{i(\omega t + kx)}, \quad (3.1)$$

$$p = A \cos(\omega t - kx) + B \cos(\omega t + kx) + i[A \sin(\omega t - kx) + B \sin(\omega t + kx)],$$

$$p_{amp} = \sqrt{A^2 + B^2 + 2AB \cos(2kx)}. \quad (3.2)$$

For two travelling waves with equal amplitudes, $A=B$, it is obvious from the last expression that a nodal point appears when $\cos(2kx) = -1$.

Sound waves are felt by the membranes of the condenser-type microphones, and the microphone produces electrical signals which are amplified in two stages before they are converted to digital readings by an analogue-to-digital conversion card. Assume that a real pressure of 1 pascal unit will read J in the computer equipped with such A/D card. Here J represents the total transfer function from the physical quantity to the final reading on the computer screen. Assume also that the waveform of the sound signal is analysed by an FFT operation to get a phase angle of θ for different signals with the same time reference point. Then the sound measured at the two microphone positions $x = -L_1, -L_2$, shown in Figure 3.1 can be represented as

$$p_1 = J_1 A_1 e^{i(\omega t + \theta_1)} = I e^{i(\omega t + kL_1)} + R e^{i(\omega t - kL_2)}, \quad (3.3)$$

$$p_2 = J_2 A_2 e^{i(\omega t + \theta_2)} = I e^{i(\omega t + kL_2)} + R e^{i(\omega t - kL_2)}, \quad (3.4)$$

where subscripts 1 and 2 represent the two microphones, and $A_{1,2}$ represents the digital readings from the two microphone channels.

The two measurements give two equations. These equations can be solved for the incident and reflective waves as follows,

$$I = \left[+J_1 A_1 e^{i(\theta_1 - kL_2)} - J_2 A_2 e^{i(\theta_2 - kL_2)} \right] / \left[e^{ik(L_1 - L_2)} - e^{ik(L_2 - L_1)} \right], \quad (3.5)$$

$$R = \left[-J_1 A_1 e^{i(\theta_1 + kL_2)} + J_2 A_2 e^{i(\theta_2 + kL_2)} \right] / \left[e^{ik(L_1 - L_2)} - e^{ik(L_2 - L_1)} \right]. \quad (3.6)$$

If a rigid plate is put at the end of the duct, $x=0$, the values of the incident and reflected sound waves are forced to be equal. This condition transforms the above solutions into the ratio of transfer functions:

$$I = R \Rightarrow \frac{J_2}{J_1} = \frac{A_1 e^{i\theta_1}}{A_2 e^{i\theta_2}} \left(\frac{e^{ikL_2} + e^{-ikL_2}}{e^{ikL_1} + e^{-ikL_1}} \right). \quad (3.7)$$

Theoretically, this is the only test necessary to find out the ratio. But a small trick can be applied to reduce the work of calculation by swapping the two microphones and take another set of readings, which are denoted by primes,

$$I' = R' \Rightarrow \frac{J_1}{J_2} = \frac{A_2' e^{i\theta_2'}}{A_1' e^{i\theta_1'}} \left(\frac{e^{ikL_2} + e^{-ikL_2}}{e^{ikL_1} + e^{-ikL_1}} \right). \quad (3.8)$$

The combination of the two results lead to

$$\left(\frac{J_2}{J_1} \right)^2 = \frac{A_1 A_1'}{A_2 A_2'} e^{i(\theta_1 + \theta_1' - \theta_2 - \theta_2')}. \quad (3.9)$$

Note that this method compromises the effect of the slightly different microphone insertion design at the two points.

Having found the ratio, the rigid plate can be removed and the microphones restored to their original insertion positions. This time, measurement can be taken to determine the ratio of wave amplitudes in a general standing wave. The incident and reflective components can be found as follows:

$$I = p_2 \frac{(J_1 / J_2) r e^{-ikL_2} - e^{-ikL_1}}{e^{ik(L_1-L_2)} - e^{ik(L_2-L_1)}}, \quad R = p_2 \frac{-(J_1 / J_2) r e^{ikL_2} - e^{ikL_1}}{e^{ik(L_1-L_2)} - e^{ik(L_2-L_1)}}, \quad (3.10)$$

where

$$p_2 = J_2 A_2 e^{i\theta_2}, \quad r = \frac{A_1 e^{i\theta_1}}{A_2 e^{i\theta_2}}.$$

Still, the absolute value of the sound wave cannot be found unless the microphone is calibrated by a piston phone which is known to produce 124dB noise for 250Hz. The result is the travelling wave amplitudes, I , R scaled to the sound pressure at any one of the two microphone positions, such as p_2 . Most of the times, it is good enough in duct acoustics to have a ratio of I/R . For example, the impedance value on the surface at $x=0$ can be determined by $Z = \frac{I+R}{I-R}$ once the ratio of I/R is known.

The results for the two microphones which will be used in fan noise measurement are shown in Figure 3.2.

3.2 Application to duct acoustics measurement

It is necessary to learn the basic measurement technique, which would be used in the future experiments. The author used the following experiments to familiarize the experiment technique which will be dominant in the latter section. Also, the

training of this section helps the author to think in detail during the experiment. Although the following section is not the core study of this thesis, it is essential to illustrate the results during the author preliminary study.

The experimental set-up for the duct acoustics is shown in Figure 3.3. The purpose of the experiment was to find out the axial phase speed of sound propagating through a duct with one flexible membrane. Theoretical prediction (Huang 2000) shows that, at low frequencies, the axial wave speed is much smaller than the normal value of $c=340\text{m/s}$ where one wall is flexible. While the reverse is true at high frequencies. This variation of wave speed with frequency is called the dispersion relationship, which will be displayed later together with the experimental data. The task now is to measure the amplitude and phase angle of sound at every point in the duct, so that the dominant wavenumber can be found by applying the space-domain FFT to the complex amplitude distribution along the duct.

A 6 inch loudspeaker driver unit with 40Hz resonance frequency was enclosed in a wooden box and was driven by a function generator and amplifier. The duct was coupled with the loudspeaker via a contraction cone. The duct had three regions: an upstream part of 75cm length with rigid walls, a test section with a 1m membrane on the lower side, and a downstream section with a 15cm rigid wall and a 90cm section filled with sound absorption material. Complete sound absorption was not expected since reflection occurred at the leading and trailing edges of the membrane anyway. The membrane was backed by a lower cavity 3.3 cm in depth to prevent breakout noise. A tensile force of 4.0N, which

produced 10% elongation of the plastic membrane, was applied. In order to best model a two-dimensional configuration, a small clearance of less than 0.5 mm was allowed between the tensioned membrane and the sidewalls of the duct. Tests with the small gap sealed were also carried out. Sound travelling over the membrane was expected to have a phase speed different from the normal speed of sound of about 340 m/s at a room temperature of 15°C. The dispersion relation was the main objective of the measurement.

Two B&K ¼ inch condenser-type microphones type number 4135 with flat amplitude response from 6Hz to 14kHz were installed flush with the duct walls: one at 37 cm upstream of the membrane, and the other on the rigid wall opposite the membrane, which was designed to slide back and forth so that all axial locations can be covered with just a few microphone insertion holes. To get the sound field of the whole length over the membrane at repeatable loudspeaker excitation, the signal taken from the “mobile” microphone over the membrane section was compared with that from the upstream microphone, which acted as a reference. The amplitude ratio and phase difference between the two pressure measurements were determined. A probe microphone B&K type 4182 with a 5cm stiff probe head of 1.24mm diameter was inserted through the sliding plate next to the ¼in. microphone. It moved along with the ¼-in microphone and was used to measure the sound pressure right above the membrane surface. The frequency response of this probe is 3 dB down from dc to 2 kHz, which is the maximum frequency required for the probe measurement. The microphones were supported by B&K’s Nexus four-channel conditioning amplifier type 2693 and the signals were fed into a Pentium II Dell computer installed with a National

Instruments AD card type PCI-MIO-16-E-1 controlled by the LabVIEW software.

The author's main contribution in the project was to recommend and implement the chirp measurement method. A chirp sound source sweeps through a certain frequency range, and it saves a lot of time comparing with doing the experiment one frequency by one frequency. Since the sound was confined inside the whole rig, it was a little uncertain as to what pace of frequency sweep was suitable for the experiment. If the sweep is too fast, the instantaneous acoustic field in different regions may feature different frequencies and the standing wave pattern found will not represent the corresponding situation when the experiment is carried out by single frequency excitation. A gradual sweep was therefore recommended through the use of three narrow frequency bands. The bands are: 50–300 Hz, 300 Hz to 2.5 kHz, 2.5–5 kHz. The sweep was linear “ramp-up” and the duration was 4, 2, and 1s, respectively. The AD card sampling frequencies were 4, 16, and 32kHz for the three bands, respectively, and data sampling was carried out over one sweep cycle. The three-band separation was necessary because the conditioning amplifier for the microphone required a different setting in order to maximize the true resolution of the A/D conversion. The spatial step for the “sliding” microphones was 2cm for low frequencies and 1cm for high frequencies. This step size was found to be sufficiently small to resolve the waveforms. For each position, the amplitude ratio and phase angle relative to the reference microphone were found at all frequencies. The data output was then sorted out in terms of amplitude and phase distribution along the

membrane for all individual frequencies. A set of harmonic excitation tests were also carried out, which confirmed the validity of the chirp measurement.

As shown in Figure 3.4, the experimental results (open squares) are compared favourably with the theoretical predictions (solid curves). Good agreement has been achieved in general. The membrane had a mass per unit length of 60g/m, and the duct had the dimension of 3cm by 3cm. A tension of 4N was applied. It is quite remarkable that wave speed as low as 8.3m/s [see Figure 3.4(b)] and as high as 1350m/s [see Figure 3.4(c)] have been found in such a simple experiment. The departure from the normal value of 340m/s over the membrane section results in a significant amount of wave reflection at the interface of the rigid and flexible sections of the duct. This mechanism is potentially very useful for duct noise control. The speed of eigenwave over the membrane may be understood from the viewpoint of the mass-spring system of the fluid-loaded membrane. At low frequencies, the effect of fluid is purely masslike and the result is a membrane heavier than its own weight. The wave speed is slower than the *in vacuo* value, which, in this example is determined by the tensile force applied. At higher frequencies the effect of fluid loading is springlike and the eigenwave is found to be faster than the speed of sound in free space. At a particular frequency the effect of mass and spring balance each other, and singular sound speed is predicted for a lossless system. The frequency at which this singularity occurs depends only on the mass ratio and close agreement with experimental data is obtained. At supersonic speed, waves travel in a way similar to the high-order modes in a rigid duct where the sound waves advance in a zig-zag path with supersonic axial wave speed.

3.3 Tachometer-triggered data acquisition system

The experimental set-up for noise measurement is illustrated in Figure 3.5, and the experiments were conducted in a fully anechoic chamber with a cut-off frequency of 80Hz. The motor was fixed inside a metal cylinder. The whole test rig was fixed using several rigid vertical supports and some vibration-absorption pads. A small accelerometer (B&K type 4374) was attached to the cylinder casing to measure the vibration. It had a diameter of 5mm and was used with B&K's conditioning amplifier Nexus type 2692. The comparison of noise measured with and without the accelerometer showed no detectable difference. In other words, the noise caused by the flow blowing through this small obstacle was insignificant. A tachometer was located on the side of the rig to make sure that there was no influence on the clean inflow condition. The white area in the top blade shown in the photograph of Figure 1.5(b) was a reflective paper for use with the tachometer. Two condenser-type microphones (B&K type 4197 used together with B&K's Nexus conditioning amplifier type 2690) were positioned symmetrically with regard to the rotational axis. The two microphones were calibrated using the method described earlier. The angular positions of the two microphones were set where the noise radiation was maximum. $\theta = 30^\circ$ was the result, and this outcome was similar to the loading noise directivity shown in Figure 1.3(d). The distance between the microphone and the impeller centre is $R=0.6\text{m}$. There were a total of 4 channels of signals to be taken to the analogue-to-digital conversion card (National Instruments PCMCIA card: PCI-1200)

which was controlled by a LabVIEW program specially written for this experiment. The four channels were tachometer, microphones 1 & 2, and the accelerometer. The background noise level was less than 40dB while the fan noise was at least 20dB higher at distance $R=0.6\text{m}$.

The LabVIEW code is displayed in Figure 3.6 and the sample data are processed and shown in Figure 3.7. The data acquisition process was triggered by the tachometer pulse which was set at 2v in rising edge. A total of around 16 impeller cycles' worth of record was taken each time. The typical sampling frequency was $F_{abs}=32\text{kHz}$ and the rotational speed is $\text{rps}=15000/60=250$. Each record has $16 \times F_{abs}/\text{rps}=2048$ points, which is convenient for FFT. The raw data is shown in Figure 3.7 with label p_{raw} . The data of each new record is added to all subsequent data records. The total number of records, N , can be set on the front panel of the LabVIEW code, together with many other parameters. Typically, $N=100$. By using the tachometer trigger, each record is guaranteed to begin with exactly the same angular position of the impeller during rotation. The result is a synchronously averaged noise and vibration signal. The averaged data was written to an ASCII file, followed by one typical raw record. The sample averaged pressure signals are shown in Figure 3.7 with label p_{av} . Through this averaging, any signal which is not related to the impeller rotation is minimized and the signal related to the rotation is kept constant. Since the average amplitude of N random numbers has the amplitude of $N^{-1/2}$, the signal to noise ratio is enhanced by 10 times when $N=100$ is used.

3.4 Basic characters of the impeller noise

It may be useful to recall the mechanism of the spectral peak at the blade passing frequency (BPF). This is illustrated by simple mathematics using the linear superposition principle. Assuming that noise from one single blade has frequency ω and a unit amplitude, the noise radiated by B blades will be

$$\sum_{j=0}^{B-1} \exp(i\omega t + ij\theta) = \frac{\sin(B\theta/2)}{\sin(\theta/2)} \exp[i\omega t + i(B-1)\theta/2], \quad (3.11)$$

where $\theta = \omega\Delta t = 2\pi/B$ is the phase angle difference between the two adjacent blades. First of all, if the noise from a single blade is a harmonic function with the rotational speed of the shaft, the phase difference between the blades is $\theta = 2\pi/B$. Then the summation result has an amplitude of $\sin\pi/\sin(\pi/B)$, which vanishes. This means that the rotational noise should not exist if the noise made by each blade is strictly identical. The sources of rotational noise include either motor vibration or non-identical flow conditions for each blade, such as the changing tip clearance around the impeller. Then, for higher order harmonics of the rotational speed, the phase difference θ multiplies by m . The expression will be

$$\sin(B\theta/2)/\sin(\theta/2) = \sin(m\pi)/\sin(m\pi/B). \quad (3.12)$$

The first non-trivial result comes when m is equal to B , which is the so-called blade-passing frequency or BPF. It is also clear that components at frequencies other than the harmonics of BPF comes from the non-identical radiation of noise from individual blades. The BPF noise comes from the B th component of the sine-transform of the single blade sound signature. If the signature is sufficiently sinusoidal, then even the BPF noise is absent. For small axial flow fans, noise

from a single blade tends to be rather sinusoidal. In other words, the amplitude at higher harmonics will be low. Therefore, it is expected that a low Gutin noise when the number of blades is big.

Eventually, the actual situation in which everything makes noise and the noise is not so sinusoidal. When the fan blades are stripped off, the motor can be run at the same speed and the noise can be recorded. The spectrum is shown in Figure 3.8 in a zoom-in view. The peak frequencies correspond to 1 through to 10 rps. The 5th harmonic is the highest and it accounts for about 55% of the total energy in the complete noise spectrum. It was discovered that the motor had 5 brushes, and the brush noise was also found to be significant when the blades were mounted.

The spectra of sample data shown in Figure 3.7 are given in Figure 3.9 for (a) two-blade impeller and (b) four-blade impeller. The comparison of the two samples can be described as follows.

- The two-blade impeller has dominant noise at blade passing frequency but the four-blade impeller is dominated by the brush noise at 5rps.
- The two-blade fan has more rotary noise than broadband noise, but the four-blade impeller may have more broadband noise than the rotary noise. This is shown clearly by the difference in amplitude between the raw and averaged signal in Figure 3.9.
- The origin of the strong broadband noise is not clear now, but it is possible that it comes from the turbulent flow. The turbulent flow should be stronger in the four-blade impeller than in the two-blade impeller.

It is further pointed out that, the contribution from the motor noise to the discrete tones may be enhanced when the impellers are mounted. It is possible that the impeller unbalance shakes the motor axis seriously, so that the actual motor noise cannot be indicated by the noise made by the isolated motor shown in Figure 3.8.

Chapter 4: Acoustic analysis

As explained in the introduction, Gutin noise has well-known mechanisms. For noise measured at two symmetrical points with respect to the rotational axis, Gutin noise should be identical if the number of blades is even. When the number of blades is odd, certain phase angle relationship should exist, but it is not so easy to implement the analysis. That is the reason of selecting a sample impeller with even number of blades.

The noise mechanism from the unsteady flow in the relative reference frame is not so clear since it is difficult to measure the flow field with a rotating part. Assuming the unsteady flow has two components. One is rotary and one is random. The random part can be filtered out by the synchronous averaging but the rotary part is not very well understood.

In this Chapter, the purpose is to separate the noise caused by the rotary vibration (see Figure 1.4) from the aerodynamic noise by using the hypothesis of equation (1.1), which is recalled here,

$$p_g = \frac{p_1 + p_2}{2}, \quad p_v = \frac{p_1 - p_2}{2}, \quad (4.1)$$

where p_1, p_2 are the noise measured at the two symmetrical microphone positions, see Figure 1.4, p_v is the vibrational noise, and p_g represents all aerodynamic noise. But it is not very clear whether the unsteady rotary noise will enter into p_g or p_v , or both. If there is no unsteady flow noise, p_g simply represents Gutin noise, which is caused by the steady flow. But, in general, p_g

may not be all Gutin noise. As far as the motor noise is concerned, there is also uncertainty. There are usually various excitation sources and propagation paths of noise in a motor. It has proven difficult to locate the vibration and noise sources with only one specific spectrum (Chen & Li 1989). To reduce the noise radiated by electric motors, it is necessary to locate exactly the dominant frequency components of the motor noise and to trace their sources. The overall motor noise, which consists of electromagnetic noise, mechanical noise, and ventilation noise, is determined by the electromagnetic design and the mechanical structure as well as the quality of the manufacture and assembly of the motor. There are usually various excitation sources and propagation paths of noise in an operating motor, so its noise and vibration spectra are rather complicated.

Bearing in mind the complex nature of noise sources, the author takes a liberal use of the phrase 'Gutin noise' for p_g and 'vibrational noise' for p_v in this chapter. The correlation of signals taken from the accelerometer [shown in Figure 1.5(b)] with both p_g and p_v is studied. The normalised correlation between two signals, say f and g , is defined as

$$\sigma(f, g | \Delta t) = \frac{\int_0^T f(t)g(t + \Delta t) dt}{\sqrt{\int_0^T f^2(t) dt \int_0^T g^2(t + \Delta t) dt}} \quad (4.2)$$

with time shift Δt as a variable. It will be shown that p_v is correlated with the vibration velocity signal from the accelerometer on the cylinder casing (using the switch of velocity output) v_c , while p_g and v_c are not so correlated.

4.1 Signal calibration and filtering

Since the signals from the accelerometer are very different from those from microphones, it is necessary to investigate the timing between them. This was performed by the following test. First, the impeller was switched off but the whole measurement system remained ready. The cylinder was struck by an object. The striking was just heavy enough to make audible noise for the microphones to pick up. The simultaneous records of noise and vibration can be compared. As shown in Figure 4.1, the accelerometer signal is very sharply timed with the striking action, but the noise signal is more complicated. The zoom-in view is provided in the lower part of the figure where the exact striking time is identified in both signals by vertical broken lines. The author argued that the noise generated has strong ringing later on because noise is radiated by the resonant vibrations of the cylinder and its connected structures. The time interval is found to be

$$\Delta t = 1.59 \text{ ms} ,$$

or 51 data points. Sound travels 0.54m during this interval, which is very slightly longer than the actual distance between the striking point and the microphone. This means that the two measurement channels have almost the same response time from the physical event to the final data capturing by the computer. The calibration seems to be trivial but one can only say so when this is confirmed.

The motor brushes causes vibration as well as making frictional noise. Since the issue of frictional noise is rather complex, it is decided to simply remove this component of the spectra by a bandstop FIR filter. Figure 4.2(a) shows the

amplitude response of a Kaiser FIR filter which filters out the low-frequency drifting of the signal, as well as the brush induced vibration and noise around 5rps. Figures 4.2(b) and 4.2(c) are, respectively, the vibration velocity signals before and after filtering. It is shown that the removal of the 5rps component is rather subtle. The filtered signals are used in the analysis of correlation, but the originals are used in the spectral plots shown in Figures 4.3 & 4.5.

Figure 4.3 compares the Gutin noise spectrum in Figure 4.3(a) and the vibrational noise in Figure 4.3(b). The most obvious difference between the two is the change of dominance between the blade-passing frequency in Figure 4.3(a) and the rotational frequency in Figure 4.3(b). The pattern of Figure 4.3(b) is rather similar to that in Figure 4.3(c) for the vibration velocity v_c . All have a prominent peak at the brush frequency of 5rps. The level of the brush noise is seen to be about equal to the Gutin noise typically concentrated at the blade passing frequency of 2rps. It is interesting to note that there is no signal in the accelerometer at 2rps. Instead, the vibration signal concentrates at 1rps. That confirms the suspicion that the fan vibrates like a waving stick as depicted in the left-hand side of Figure 3.5.

4.2 Correlation studies

Figure 4.4 shows the normalized correlation as a function of the shift index. The reason why the index is shifted is that there must be a time delay from the time the vibration occurs and the time the noise arrives at the two microphone positions. Detailed calibration between these two instruments was done in the

last section, but the author still wants to show the correlation as a function of the time difference to confirm the pattern. The solid line is for the correlation between the vibration velocity v_c and the vibration noise p_v . The maximum correlation of 0.924 is found when the shift is 44 sampling points or 1.375ms in which sound travels a distance of 47cm. This distance is indicative of a direct relationship between the surface vibration and the vibration noise sensed by the microphones if the two types of sensors have the same response time. This result differs slightly from that of the striking test, but the two are close enough. Two factors make this comparison a satisfactory one. First, there is uncertainty as to the exact sound reception at the microphone position as shown in the lower half of Figure 4.1. Second, the correlation index remains rather high around the shift index of 51 found in the striking test.

The dashed line in Figure 4.4 is for the correlation between the Gutin noise p_g and the vibration velocity v_c . There is hardly any correlation for these two (0.0093 at shift 44). This result is a clear vindication of our assumption of rigid-body vibration of the fan and the phase-angle directivity of the noise induced by such a vibration. Notice that the brush noise and brush vibration are filtered out for the correlation studies. Otherwise the two correlation indices will be rather close to each other since both p_g and p_v are correlated with the vibration source having a circumferential pattern of five.

Figure 4.5 shows the results for a four-blade fan. Notice that the two-blade fan used earlier was made by cutting away two blades from this four-blade fan. Figure 4.5(d) shows clear peaks of vibration velocity at 1rps and 5rps. The

former is indicative of a swinging vibration of the fan body, while the latter is clearly the brushing effect. Figure 4.5(a) shows that the brush noise is dominant in a raw noise sample, and more so in the averaged Gutin noise spectrum of Figure 4.5(b). Contrary to normal expectations, the noise at the blade-passing frequency of 4rps does not appear as the dominant. It means that reduction in aerodynamic noise in this case is unlikely to result in any substantial acoustic benefit. Both Figures 4.5(c) and 4.5(d) show clear dominance of signals at the rotational frequency. This is an indication of the rigid-body vibration of the fan. The normalized correlation between p_v and v_c is 0.81, while that between p_g and v_c is merely 0.018. The maximum correlation occurs at the delay index of 54, which is 10 more than the two-blade fan. The difference is probably caused by the fact that the two microphones are not, strictly speaking, placed in the far field.

In terms of noise sources, the following conclusions are drawn. For the 2-blade impeller, Gutin noise dominates. However, the vibration noise dominates the 4-blade impeller.

4.3 One-microphone method

In this section, a method using one-microphone for the analysis of correlation is described. If the noise made by the rotor depends on the rotation only, then the signal should repeat its pattern at the blade passing frequency. In other words, the pattern should repeat itself once per $\frac{1}{4}$ cycle for a four-blade impeller. If this is the case, the signal measured at microphone 2 located at an angle θ away from

microphone 1 should be identical to the signal of microphone 1 but with a time delay of θ/ω where ω is the angular speed. In this way, the signal at the second microphone can be derived from that of the first microphone, and there is no need to use the second microphone in the actual test. In making this statement, one is assuming that the noise radiated is uniformly around the rotating disk and there is no element which is not dependent on the fan rotation. The comparison of analysis using this assumption with that of the real two-microphone method will serve as an indication of how accurate the real situation satisfies the above assumption. The signal shifted by half a cycle as the second signal is used. The 2-blade and 4-blade impellers are used as follows.

Figure 4.6 shows the results of time-domain signal and the spectrum of the 2-blade impeller running at 15000rpm by using the one-microphone method. The original signal, p_1 , has around 1 volt peak-to-peak, but 0.5 volt is left when the vibrational noise p_v is derived from the phase-shifting method:

$$p_v = p_1(t) - p_1(t + \pi/\omega). \quad (4.3)$$

The spectra of the Gutin noise, and the vibrational noise differ a lot. The harmonic peaks are mainly with the even numbers for the Gutin noise spectrum. On the contrary, the vibrational noise spectrum features odd number harmonic peaks. For the Gutin noise spectrum, the BPF noise has around 80% of the whole spectrum energy. For the vibrational noise, the contribution is quite uniformly distributed over many odd number harmonics.

The question now is how much of the vibration noise correlates with the accelerometer. Figure 4.7 shows the correlation indices between the accelerometer signal with the vibrational and Gutin noises. It shows that the vibrational noise is highly correlated with the accelerometer signal, while the Gutin noise is hardly correlated with the accelerometer signal at all. This conclusion is the same as that reached earlier using the two-microphone method, as shown in Figure 4.4. The BPF noise dominates the Gutin noise, and the vibrational noise is correlated with the accelerometer signal.

For the 4-blade impeller, the results are shown in Figure 4.8. The overall amplitude of the signal is around 1 volt peak-to-peak, the Gutin and vibrational noises have similar amplitudes. Gutin noise shows peaks in the even number harmonics, and the vibrational noise shows odd number harmonics. This is similar to the two-blade impeller. For the Gutin noise, the BPF noise dominates the whole spectrum with a noise level of 53dB. However, for the vibrational noise, the peak at rps is 60dB. For the overall spectrum, it shows that the dominating noise is from vibration.

The correlation indices are shown in Figure 4.8. The correlation index of the accelerometer signal with the Gutin noise is only 0.1, while that with the vibrational noise is roughly 0.7. The conclusion again agrees with the analysis conducted using the signals from two microphones.

The reason for the odd and even number harmonics is a mathematical one. When a sinusoidal signal is shifted by half a cycle, the summation and subtraction will generate the pattern of even and odd peaks. The fact is that the phase shifting

method cannot reveal the full details of the phenomenon, but the important point is the correlation index between them. The index reflects the general relationship of two signals. So, for the separation of noise source, phase shifting is not a good method but can be used for the examination of the relationship between the signals.

By using the one-microphone phase-shifting method, it is clear that it is wrong to assume that the two microphone signals are identical. If it were identical, the sum of the two signals would create the same feature as the one from the phase shifting. However, the comparison of results in this section with those of the previous one does not support this assumption. So, the only reason is that the two microphone signals for Gutin noise are not identical in reality. They must have some difference. This kind of difference may be due to the experimental configuration or the general properties of the noise directivity. Some unknown noise mechanism may have its own directivity and it corrupts the directivity of the Gutin and vibrational noises, leading to an unsymmetrical pattern at the two microphones. Similar phenomenon was observed by Quinlan (1992) and Lauchle et al (1997), but so far no plausible explanation has been found.

4.4 Variation with rpm

It was earlier assumed that the vibrational noise is caused by the rigid-body, eccentric rotation of the motor-impeller assembly. If this is the case, it may be possible to model this noise source as a simple oscillating wire. The wire model is used in textbooks, such as (Morse 1968), as a physical model for a two-

dimensional dipole. The total power radiated per unit length of the vibrating wire is expressed as follows,

$$P = \frac{4\pi^5 f^3 \rho_0 R^4 U_0^2}{c^2}, \quad (4.4)$$

where f is the frequency, R is the cylinder radius, U_0 is the velocity amplitude of the oscillating cylinder, and c is the speed of sound. It would be interesting to check whether it is possible to relate the power law shown in this crude model with the measured data of sound power versus vibrational information picked up by the accelerometer. This is done by plotting the total radiated power normalized by the vibration energy, P/U_0^2 as a function of the rotational frequency and see whether the dependency follows the cubic power law: $P/U_0^2 \propto f^3$ where f can be represented by the rpm. The sound power is crudely represented by the square of the measured sound pressure level and the amplitude of the vibration velocity is found by using the velocity output mode in the Nexus conditioning amplifier.

Figure 4.10 is the result of this study. The frequency is represented by the rpm, the vertical co-ordinate represents the ratio of sound power over vibration energy sensed by the accelerometer. The rotational speed tested ranges from 8000 to 15000rpm. It seems that the two regions of extreme rpm have quite different features from the central region. For the region of rpm from 9k-12k, a curve fitting shows a power-law with exponent 3.37, which is slightly higher than the expected value of 3.0. In other words, the result for the whole range does not match with the prediction. However, the speed range of 9000rpm to 12000rpm seems to agree with the cubic law very well.

As a matter of information, The results of the comparison of Gutin noise and vibrational noise as a function of rpm as well as the distance between the impeller and the microphones are included. There is no theoretical prediction to compare with in this case. But an observation will be made out of these data. The results are displayed in Figures 4.11 and 4.12 for the 2-blade and 4-blade impellers, respectively, with legends explained in the caption of Figure 4.11.

For the 2-blade impeller, either Gutin noise or vibrational noise can dominate. For example, for the measurement distance of 1m, the vibrational noise is higher than the Gutin noise in the rotational speed region from 9000 to 12000rpm. However, for rotational speeds higher than 12000rpm, Gutin noise becomes the main contribution. For the measurement distance of 0.6m, the vibrational noise also dominates before 9000rpm. Beyond that rpm, Gutin noise takes over. For the near field measurement at the distance of 0.3m, Gutin noise is higher than the vibrational noise. But in the region from 8000 to 9000rpm, the two are roughly equal.

For the 4-blade fan, the measurements were carried out at three distances, 0.3, 0.6, 1m respectively. For the measurement distance of 1m, the contribution of the vibrational noise is higher than Gutin noise except for the rotational speeds from 11500 to 14000rpm. Gutin noise is dominant within that region. For the measurement distance of 0.6m, the vibrational noise is always dominant. However, for the rotational speed from 12000 to 13000, the two become equally

important. The vibrational noise is dominant beyond this region. Similar trends are observed for the near field measurement distance of 0.3m as those for 0.6m.

Chapter 5: Noise abatement

5.1 Introductory remarks

The efforts of reducing the hair dryer fan noise actually began before the details of the flow field and acoustic field were analyzed due to the limitation of instrumentation at the beginning of the project. The attempts to reduce noise were entirely based on simple physical intuition before the author learned more about the fan noise. In other words, it had elements of trial-and-error. Having said that, the current understanding is still very limited. It is generally agreed in literature that not all fan noise generation mechanisms are understood. In the case of this project, the detailed knowledge is limited to the isolated fan impeller. What happens inside a real machine equipped with a ventilation fan, such as the one shown in Figure 1.5(a), is a much more complicated issue. Specifically, the real fan noise has a rich variety of noise sources related to the unsteady and turbulent flows:

- A lot of noise must be generated by the turbulent inflow through the finger protection grid. This turbulence will interact with the rotating impeller. This is known to be one of the most powerful noise mechanisms. Details were described in Chapter 1.
- After the flow comes out of the impeller, it will hit the stationary guidevane and this is also a powerful interaction noise. In fact, it is

regarded as the main noise source in large, multi-stage turbomachines used in aerospace applications.

- Further downstream, noise is also created by the interaction of the turbulent wake flow with the heating elements

Given such background, one realizes that the efforts in reducing fan noise will continue to be guided by physical intuitions as opposed to the detail analysis either by experiments or computation. It is in this sense that the inclusion of these earlier efforts would not be completely out of place(Martin 1993). Three methods are described in the following sections, with the last two being more successful.

5.2 Effect of changing the guidevane in the hair dryer

Normally, when the rotational speed decreases, both noise and flow rate will reduce. That points to an important approach of fan noise reduction described as follows. If the design of the fan can be improved such that it works much more efficiently, the required volume flow rate with a given loading of pressure difference may be achieved with a slower rotational speed. Then noise will almost certainly decrease. This approach will work in many cases when the fan in question is produced at very low cost, designed incorrectly or installed incorrectly. According to the author's experience, many small manufacturers lack their own expertise in turbomachinery design and they simply copy the fan blades from other products or similar products designed by other companies. It is likely that there is subtle differences that they are not aware of, leading to wrong

designs. Bearing in mind this possibility, a hair dryer fan like the one shown in Figure 1.5(a) is selected for analysis. The velocity triangle analysis in section 2.2 indicated that the incidence angle is over 10° for both the impeller and the guidevane at 15000rpm. That means the machine may not be designed properly for the desired operation mode. Either the impeller or the guidevane can be modified. Since the latter was easier to access, steps were taken in this direction first.

The number of the guide vanes is modified so as to (a) reduce the possible blockage on the airflow, and (b) reduce the opportunity to generate interaction noise. The number of vanes was reduced from 12 to 6 and 3. It was an easy set of numbers that can be cut down step by step. It is suspected that extra noise came from the vortex shedding after the trailing edges of the impeller blades.

The near field noise was measured at a position which was 10cm away from the rotational axis and 10cm upstream from the rotational plane. Scientifically, this point is within the near field ($kr \ll 1$), and the near field is complicated. The sound power radiated to the far field cannot be estimated by the sound pressure level measured in the near field. The short distance was chosen due to the practical interest. The component of the near field can be strong due to the dipole nature of the fan noise.

Figure 5.1 shows the comparison between flow performance of the fan with different number of vanes. The result shows that 12 blades are too many but 3 will be too few. The optimal is 6. The 6-blade guidevane increases the volumetric flow rate by 3-5% at the same rotational speed. Hence, it can reduce

the rotational speed from 15000 to 14000rpm in order to achieve the same flow rate. The measurement of noise against rpm is shown in Figure 5.2. The change from 15000rpm for 12 vanes to 14000rpm with 6 vanes is only 1dB. But the change is more sensitive in the region of low rpm. The 6-blade guide vane will be very quiet when it operates at a low rotational speed, such as 12000rpm. The noise level is only 77dB compared with nearly 81dB for the original design. The repeatability of the experiment was satisfactory. The difference between the volumetric flow rate against the rotational speed during different experiment times was from 8% to 12%. Moreover, the uncertainty range of the measurement of noise level against rotational speed with different numbers of guide vane was $\pm 0.2\text{dB}$. The instrument was well-calibrated to ensure the reliability of the experimental results.

5.3 Effect of changing the impeller tip clearance

Another approach to improve the aerodynamic performance is by reducing the tip leakage loss. The ratio of tip clearance to impeller radius is much higher in this fan than in large fans used in other applications. Therefore a significant improvement is expected if the gap can be narrowed. The current gap is about 2-3mm. This can be reduced by attaching a paper strip around the tip of the blade. This is only a temporary, quick-fix method, and the result may not reflect the full potential of this method. The important concern here is that whether the fan is still safe to operate when the gap is reduced. The attached paper was very light and flexible. So that the problem of safety did not occur at least in the test. Of course, a paper tip design is not practical in real hair dryer operation. The

purpose of the test was mainly focused on the potential aerodynamic and acoustic gain of this approach. If the gain is substantial, refined methods can be investigated in the future. The schematic diagram of the modification of the tip clearance is shown in Figure 5.3.

There was still some minor risk involved in the quick-fix test. The increased blade tip may increase the loading on the motor. Also, if the paper tip touches the casing, it will create serious friction and may cause a little damage to the sample. The test showed that the loading was indeed increased, as expected. The rotational speed can be decreased to achieve the same volumetric flow rate. The following table summarizes the experimental results

Table 2 The Summary of the tip clearance

	Original	Modified
Tip clearance (mm)	2-3	1-2
Rotational speed (rpm)	15000	13800
Volumetric flow rate (m ³ /s)	0.046	0.046
Noise level (dB(A))	83.6	81-85

First, the volumetric flow rate of 15000rpm was achieved at a much lower rotational speed of 13800rpm with the modified impeller. However, the noise level can be either increasing or decreasing depending on the degree of care applied in fixing the attachment. When it's attached very uniformly, the noise was reduced as much as 3dB. But when the tip was not attached carefully, the noise was increased by a similar amount. At first, this outcome was a little puzzling. Careful observation showed that the noise was generated by the attached paper scratching the casing. The spectral comparison of the original fan

with the successful blade tip modification is shown in Figure 5.4. The main improvement is that the very high peak at BPF in the original sample is replaced by two lower peaks at BPF and its first harmonic.

5.4 Effect of adding perforated sheet

The most reliable method of noise control seems to be the absorption of sound. For example, one can make use of the general idea of acoustic resonance to increase the effectiveness of sound absorption. The main difficulty of doing anything like a quarter wavelength resonance is that the duct housing the fan is too short. Therefore the perforated panel was chosen to achieve the purpose of noise reduction. An isolated paper cone was originally used in the hair dryer to be a thermal insulator for safety purposes. The idea of perforated wall was tested by digging a lot of small holes with a random pattern following the theoretical guidelines of Maa (1998) who pioneered the technique of microperforated panel absorber. The design is shown in Figure 5.5.

After enclosing the fan by the perforated panel inside the hair dryer, the noise level and volumetric flow rate were tested under the otherwise identical condition. Note that the heating element was removed throughout the test, and the problem of thermal insulation was sidelined at this stage. The purpose was that, if the idea was successful, another layer of paper cone can easily be added to guarantee the thermal performance. As far as the acoustics performance is concerned, the perforated panel may be made of any material from cardboard,

plastic, plywood to sheet metal, with any finishing or decoration to suit the purpose.

The comparison of the near field noise radiation is shown in Figure 5.6. There was a very significant achievement at the blade passing frequency. 5dB reduction was found for the highest peak at 1kHz, smaller reduction was also found for its harmonics. The total noise reduction was around 2dB. Although the reduction in the total dB level was small, the important thing is that the new spectrum appears to be flat and the noise will be more pleasant to hear and more acceptable.

Finally, an all-round comparison of one-third octave band spectra is presented in Figure 5.7 for the original fan, the fan treated with flexible tip attachment, and the fan with the perforated wall casing.

Chapter 6: Discussions

The results of this project highlight the importance of vibration induced noise for small axial flow fans used in consumer products which often suffer from the lack of dynamic balance. In order to develop a methodology of separating the vibrational noise from the noise of aerodynamic origin, an idealistic set-up was used in which the number of fan blades was even and two microphones measured sound at two opposite sides near the fan rotational plane. If the fan vibration is predominantly a rigid-body vibration caused by the structural imperfection or unsteady aerodynamic force, it is speculated that the far field noise radiated by this vibration should have an anti-phase relation at the two microphone positions, while the Gutin noise should have an in-phase relation. The sum and the difference of the two sound signals can therefore be used, respectively, to represent the Gutin and vibrational noise. This hypothesis is clearly vindicated by the very high correlation between the vibrational noise and the vibration velocity found from the accelerometer measurement on the motor casing. On the other hand, the correlation between the Gutin noise and the vibration velocity is rather low, as expected.

The motor brushes are found to cause a major vibration at the frequency of 5rps. The associated friction noise is found to be dominating for the four-blade impeller and is as important as the noise at the blade-passing frequency for the two-blade fan. This is a clear indication that the issue of the small fan noise is more complicated than in large turbomachines where aerodynamic noise

dominates. Control or removal of fan vibration becomes a very important issue. This issue is shared by many noise engineers working on fan and motor noise. The contribution of this project is the introduction of correlation study after filtering out the brush effects, which leads to the isolation of the rigid-body vibration of the fan when the blades are not dynamically balanced or when the fan is working in a condition of non-uniform inflow causing non-uniform loading around the circumference.

A few attempts were also made to reduce the fan noise in a real situation of hair dryer. Two methods were successful. One was the improvement of aerodynamic performance by controlling the tip leakage flow. For the same rotational speed, the flow rate was increased by 10% when the clearance was reduced from 2-3mm to 1-2mm. Alternatively, for the same given aerodynamic duty, the fan can satisfy the requirement at a lower rotational speed. For the sample fan, it achieved the performance of 15000rpm when it ran at 13800rpm with the tip modification. This led to reductions in noise emission. The second method was the direct absorption of noise by a perforated paper cone. Although the area of noise absorption was so limited inside the hair dryer, significant improvement was still obtained. The tonal noise was reduced by at least 5dB while the overall noise by 2~3dB. The reduction of tonal noise is very important and is indeed the main goal of this fan noise project.

In the future, the one-microphone measurement method should be further developed. The reason is the following. The existing symmetric directivity pattern of noise is only valid for a rotor with even number of blades. However,

when the fan has odd number of blades, the noise is not symmetric. In addition, the current noise abatement method used in the real product showed a good achievement. This potential needs to be harnessed in product development.

Chapter 7: Conclusions

1. The far field noise radiated by the vibration has an anti-phase relation at two microphone positions, while the Gutin noise has in-phase relation. A method of separating the aerodynamic and vibrational noises is introduced and validated by the correlation studies.
2. The vibration induced noise is often important or even dominant for small axial flow fans. The motor brushes are the main source of vibration as proven by the experimental data.
3. By tip clearance control, the noise was reduced without affecting the flow performance.
4. By using the perforated paper cone, the tonal noise was reduced by 5dB while the overall noise by 2 to 3dB.

Acknowledgements

I am very grateful to my supervisors, Dr. Lixi Huang for his supervision of this project, and Prof. R. M. C. So for his general encouragement and support. My gratitude also goes to Dr. R. J. Cao of Shantou University for his help in fan noise analysis. I thank our laboratory technician, Mr C. N. Tang, for his much help. I would also like to thank many of my friends and peers, Mr Zheng Meng-Wei, Miss Choy Yat Sze, Mr. Zhang Hong Jun, for their support on my laboratory and computational work.

References

1. LEO L. BERANEK, Noise and vibration control engineering. John Wiley & Sons, Inc. (1992).
2. J. M. BROOKFIELD, I. A. WAITZ, Trailing-edge blowing for reduction of turbomachinery fan noise, J. Propulsion & Power, Vol. 16(1), pp.57-64 (2000).
3. XINZHO CHEN & DENGXIAO LI, A study of identifying the sources of dominant frequency components of electric motor noise, Noise Control Engineering Journal, Vol. 33(1), pp.11-15 (1989).
4. A. D. D. CRAIK, Wave interactions and fluid flow. Cambridge University Press (1985).
5. J. E. FLOWCS WILLIAMS & D. L. HAWKINGS, Theory relating to the noise of rotating machinery, J. Sound & Vibration, Vol. 10(1), pp.10-21 (1969).
6. J. M. FITZGERALD & G. C. LAUCHLE, Reduction of discrete frequency noise in small, subsonic axial-flow fans, J. Acoust. Soc. Am., Vol. 76(1), pp.159-167 (1984).
7. T. FUKANO, Y. TAKMATSU & Y. KODAMA, The effects of tip clearance on the noise of low pressure axial and mixed flow fans, J. Sound & Vibration, Vol. 105(2), pp.291-308 (1986).
8. C. H. GERHOLD, Active control of fan-generated tone noise, AIAA J., Vol. 35(1), pp.17-22 (1997).

9. L. GUTIN, On the sound field of a rotating propeller, Phys. Z. Sov. Un 9, 57. Trans. N.A.C.A. Tch. Memo 1195 (1948).
10. D. B. HANSON, Spectrum of rotor noise caused by inlet guide vane wakes, J. Acoust. Soc. Am., Vol. 55(6), pp.110-126 (1974a).
11. D. B. HANSON, Spectrum of rotor noise caused by atmospheric turbulence, J. Acoust. Soc. Am., Vol. 56(1), pp.110-126 (1974b).
12. L. HUANG, Y. S. CHOY, R. M. C. SO & T. L. CHONG, Experimental study of sound propagation in a flexible duct, J. Acoust. Soc. Am., Vol. 108(2), pp.624-631 (2000).
13. GERALD C. LAUCHLE, JOHN R. MACGILLIVRAY & DAVID C. SWANSON, Active control of axial-flow fan noise, J. Acoust. Soc. Am., Vol. 101(1), pp.341-349 (1997).
14. R. E. LONGHOUSE, Noise mechanism separation and design considerations for low tip-speed, axial flow fans, J. Sound & Vibration, Vol. 48(4), pp.461-474 (1976).
15. R. E. LONGHOUSE, Vortex shedding noise of low tip speed, axial flow fans, J. Sound & Vibration, Vol. 53(1), pp.25-46 (1977).
16. R. E. LONGHOUSE, Control of tip-vortex noise of axial flow fans by rotating shrouds, J. Sound & Vibration, Vol. 58(2), pp.201-214 (1978).
17. MARTIN V. LOWSON, Applications of Aero-acoustic analysis to wind turbine noise control, Wind Engineering, Vol. 16(3), pp.126-140 (1993).
18. DAH-YOU MAA, Potential of microperforated panel absorber, J. Acoust. Soc. Am., Vol. 104, pp.2861-2866 (1998).

19. S. J. MAJUMDAR & N. PEAKE, Noise generation by the interaction between ingested turbulence and a rotating fan, J. Fluid Mech., Vol. 359, pp.181-216 (1998).
20. B.D. MUGRIDGE, Axial flow fan noise caused by inlet flow distortion, J. Sound & Vibration, Vol. 40(4), pp.497-512 (1975).
21. D. A. QUINLAN, Application of active control to axial flow fans, Noise Control Eng. J., Vol. 39, pp.95-101 (1992).
22. N. M. RAO, J. W. FENG, R. A. BURDISSO & W. F. NG, Experimental demonstration of active flow control to reduce unsteady stator-rotor interaction, AIAA J., Vol. 39(3), pp.458-464 (2001).
23. D. F. SCHARF & T. J. MUELLER, An experimental investigation of the sources of propeller noise due to the ingestion of turbulence at low speeds, Experiments in Fluids, Vol. 18, pp.277-287 (1995).
24. J. C. SIMONICH, D. C. MCCORMICK & P. L. LAVRICH, Role of leading-edge vortex flows in prop-fan interaction noise, J. Aircraft, Vol. 30(2), pp.255-261 (1993).
25. R. TRUNZO, B. LAKSHIMINARAYANA & D. E. THOMPSON, Nature of inlet turbulence and strut flow disturbances and their effect on turbomachinery rotor noise, J. Sound & Vibration, Vol. 76(2), pp.233-259 (1981).
26. I. A. WAITZ, J. M. BROOKFIELD, J. SELL & B. J. HAYDEN, Preliminary assessment of wake management strategies for reduction of turbomachinery fan noise, J. Propulsion & Power, Vol. 12(5), pp.958-966 (1996).

27. K. B. WASHBURN & G. C. LAUCHLE, Inlet flow conditions and tonal sound radiation from a subsonic fan, Noise Control Eng. J., Vol. 31(2), pp.101-110 (1988).
28. S. M. YAHYA, Turbines compressors and fans. Tata McGraw-Hill (1983).
29. PHILIP M. MORSE, Theoretical Acoustics. McGraw-Hill (1986)

Figures

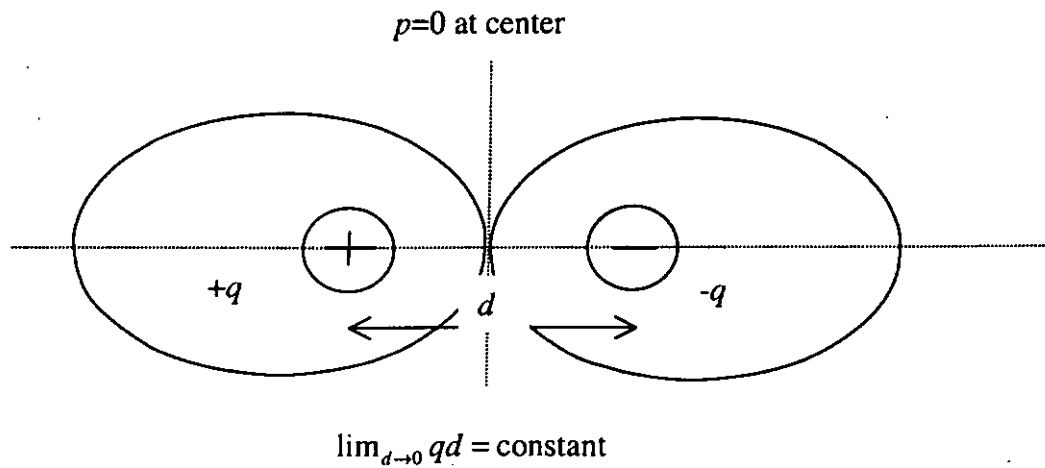


Figure 1.1: Illustration of the conceptual dipole as a limiting process of two monopoles, and the directivity of the dipole source.

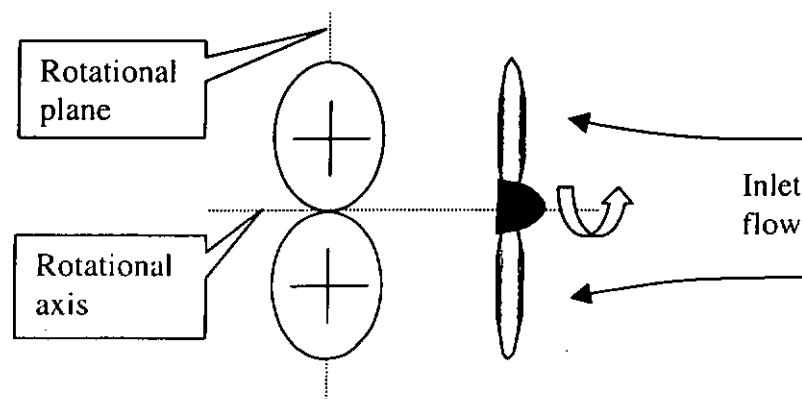


Figure 1.2: Directivity of thickness noise.

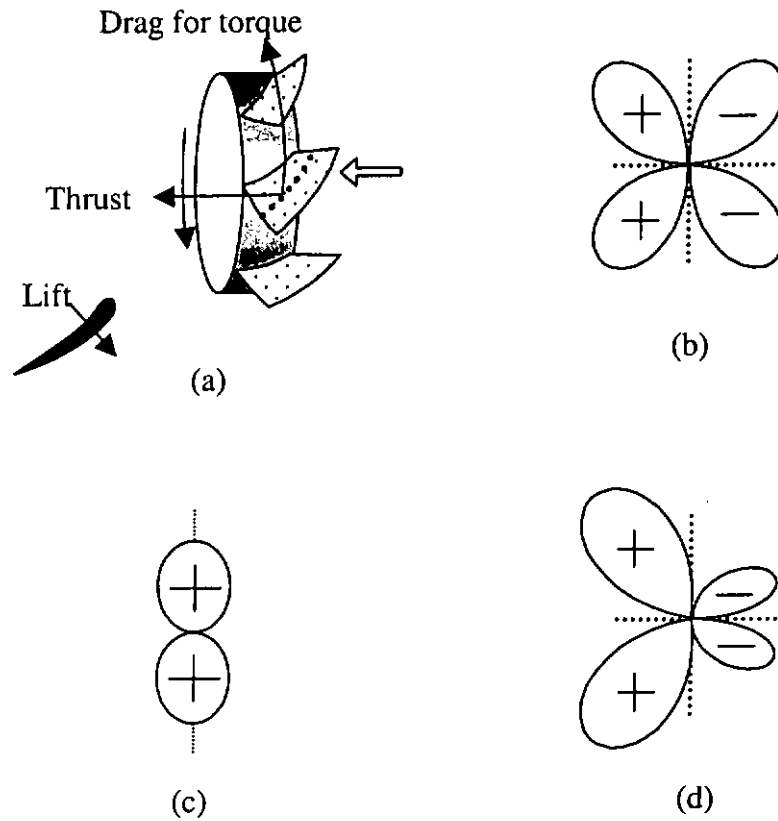


Figure 1.3: Noise generated by the steady loading on rotating blades. (a) shows the separation of loading on each blade cross section, (b) is the directivity of noise caused by the rotated thrust force, (c) shows the directivity of the torque noise, and (d) is the directivity of the total steady loading noise.

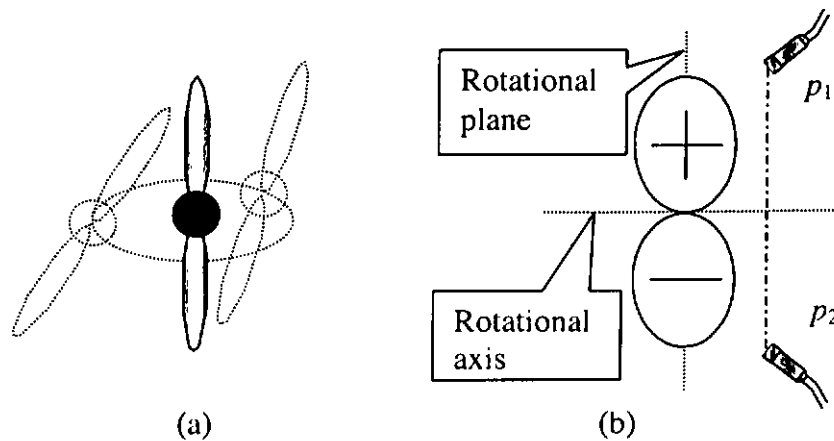


Figure 1.4: Noise radiated by the rigid-body vibration of the motor-fan assembly. (a) is the front view of the fan blades with the assembly vibration following an elliptic path (exaggerated), (b) shows the directivity of the far field sound on the side view.

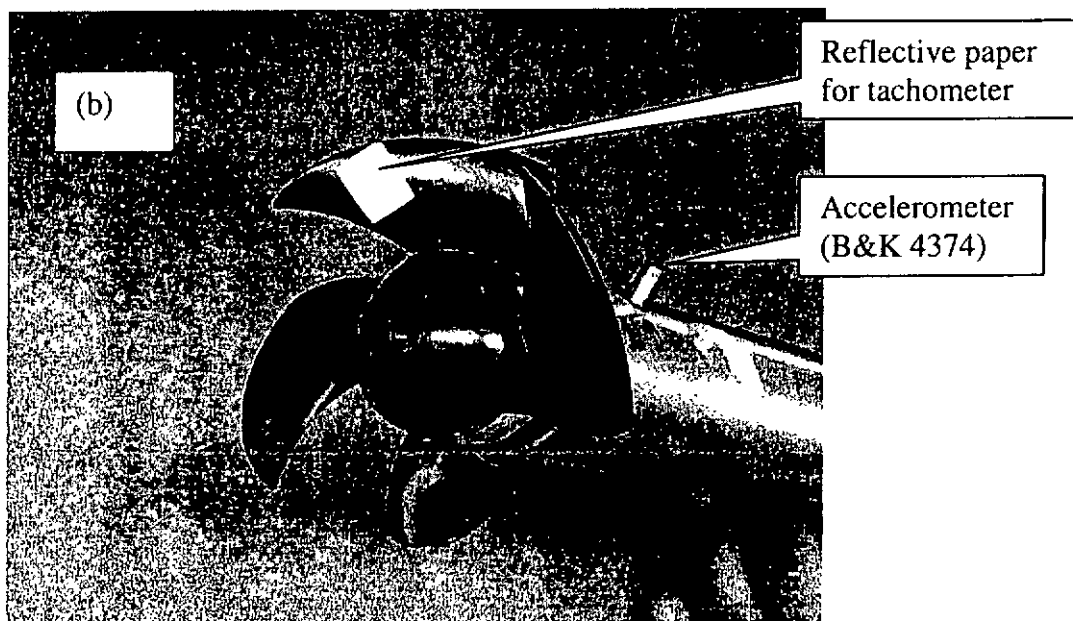
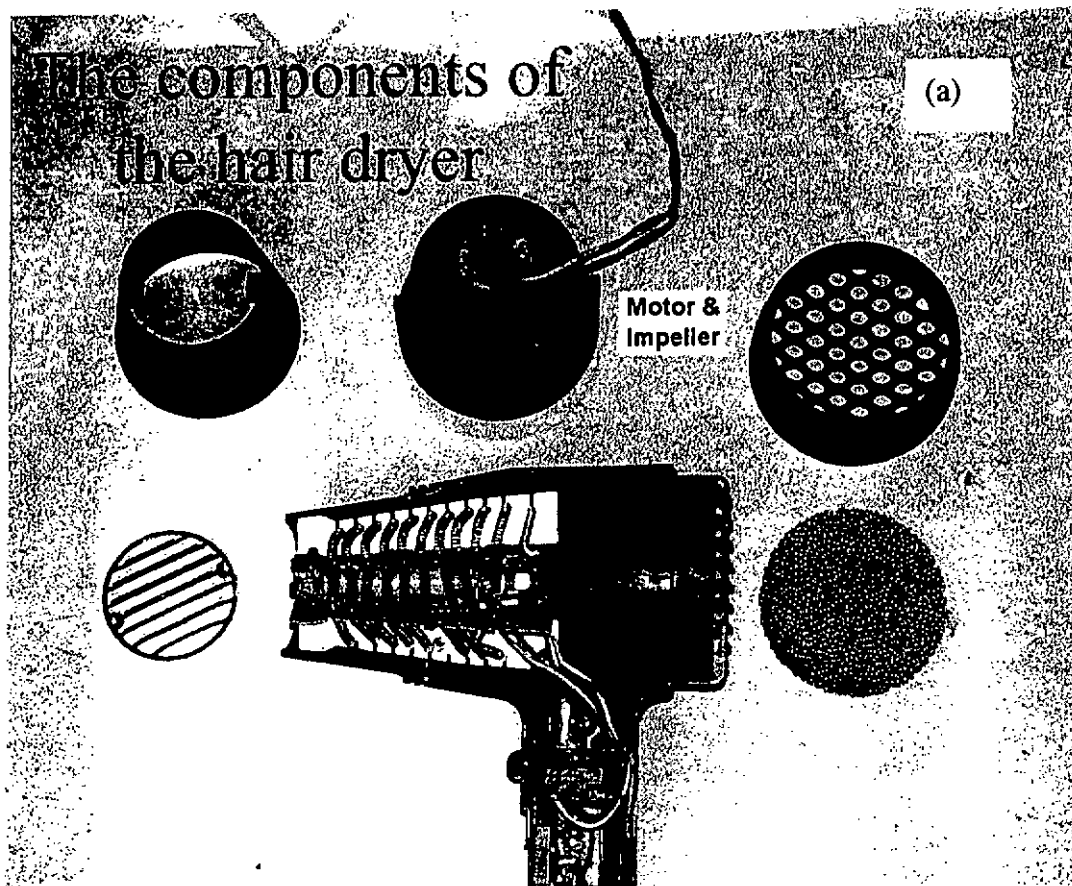


Figure 1.5: Photographs of the sample hair dryer fan used in the study. (a) is the complete hair dryer fan, (b) is the isolated impeller driven by the motor housed in a metal cylinder.

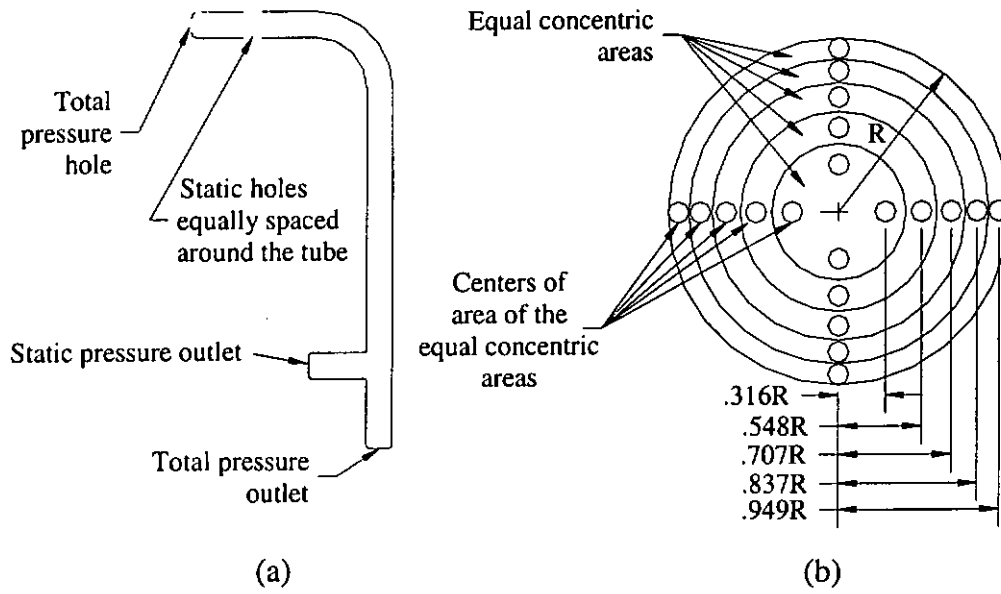


Figure 2.1: The Pitot-tube measurement of the flow through a tube. (a) illustrate the principle of the Pitot-static tube, (b) shows the arrangements of the measurement points over a circular cross section.

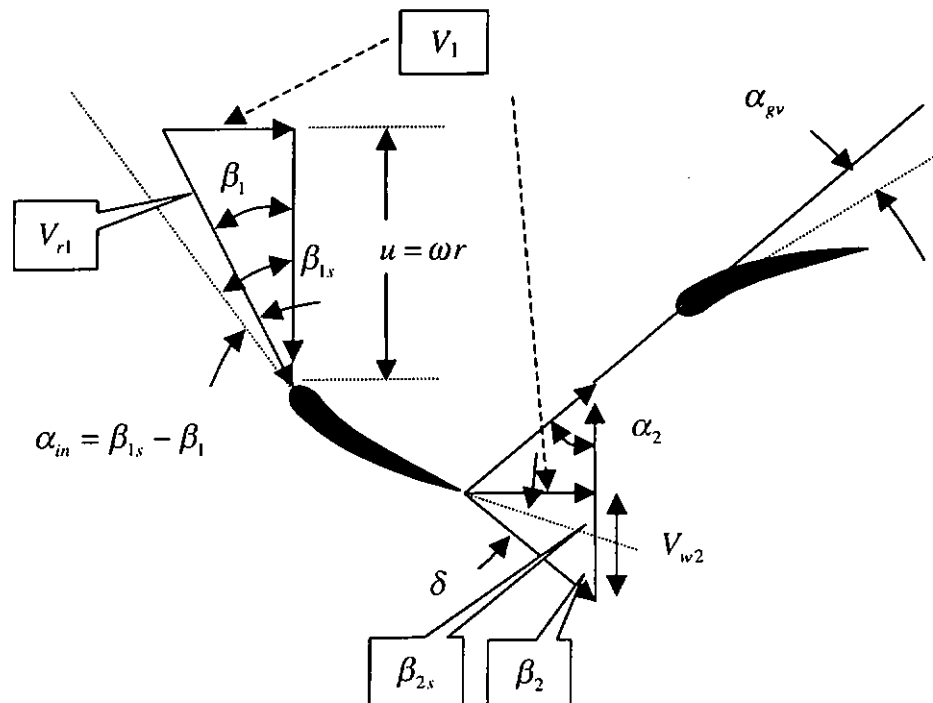


Figure 2.2: The velocity triangle analysis for a fan impeller.

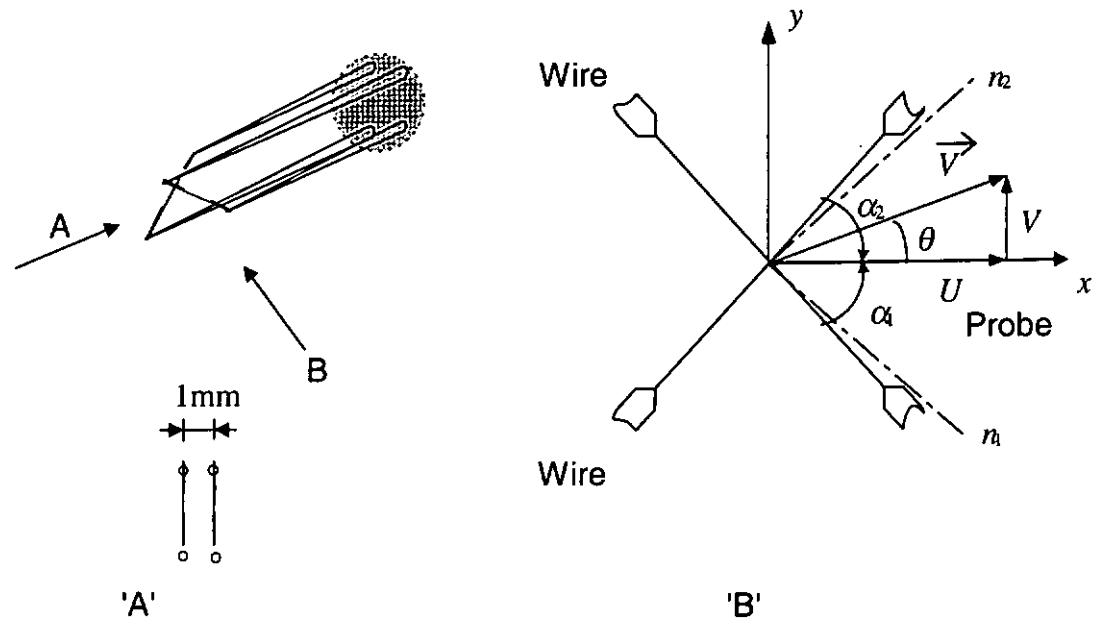


Figure 2.3: The x-wire probe.

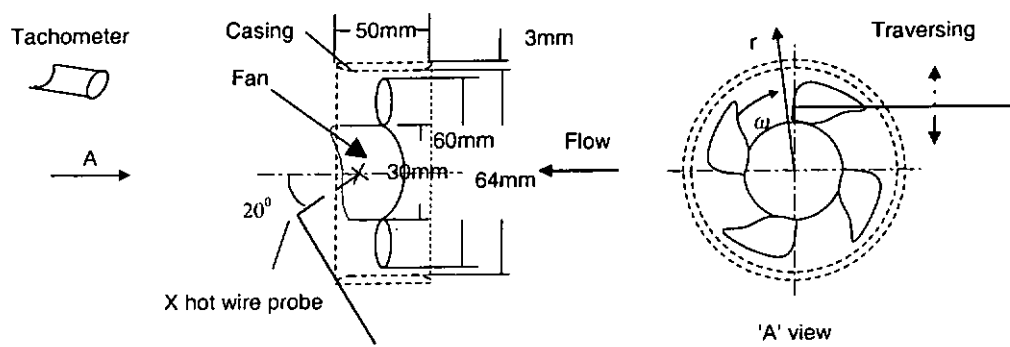


Figure 2.4: X-wire measurement for the axial and circumferential components of the absolute flow velocity downstream of the impeller.

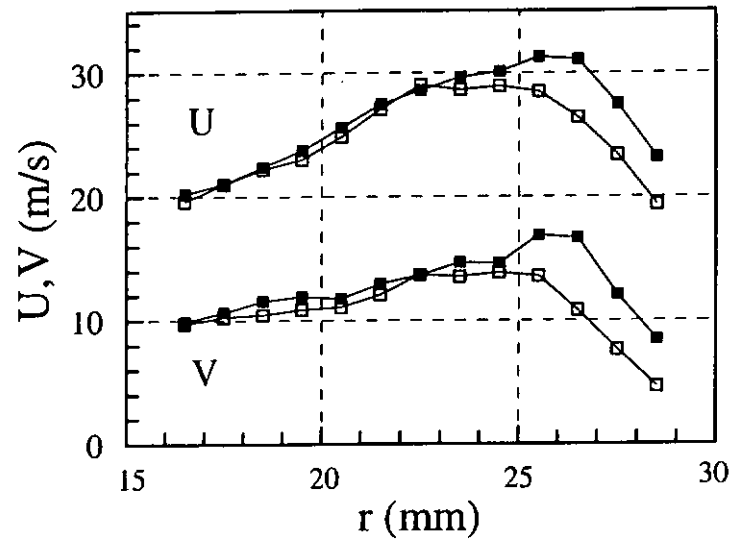


Figure 2.5: Distribution of X-wire measured average flow velocity in axial (U) and circumferential (V) directions for two values of tip clearance: 1mm(solid squares) and 2mm (open squares).

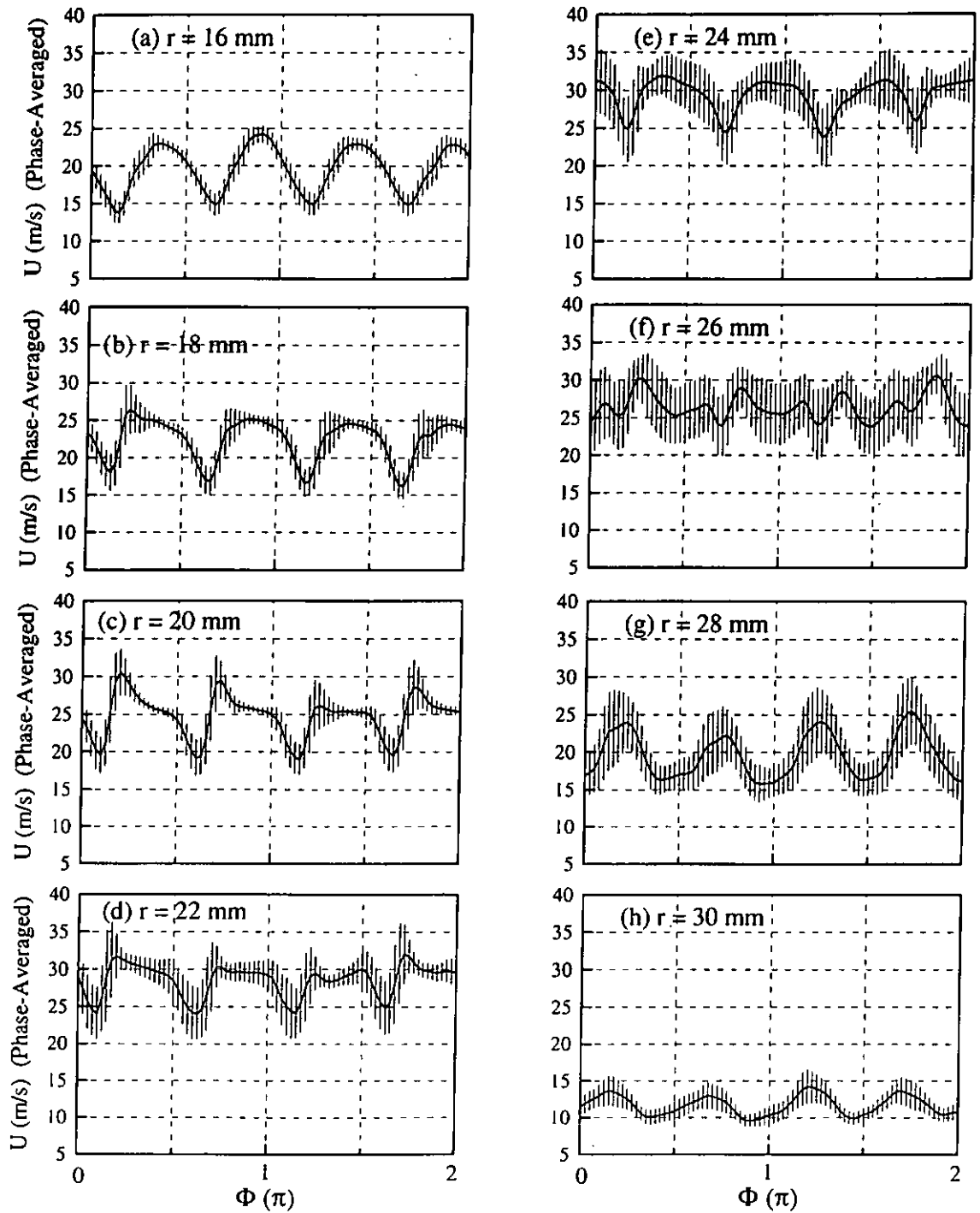


Figure 2.6: Distribution of local average of the axial flow velocity (solid curves, viewed from ground) and its standard deviation (vertical bars, over 500 cycles of measurements). The observation point has the angular position of Φ fixed to the impeller and the radial position is marked on each graph.

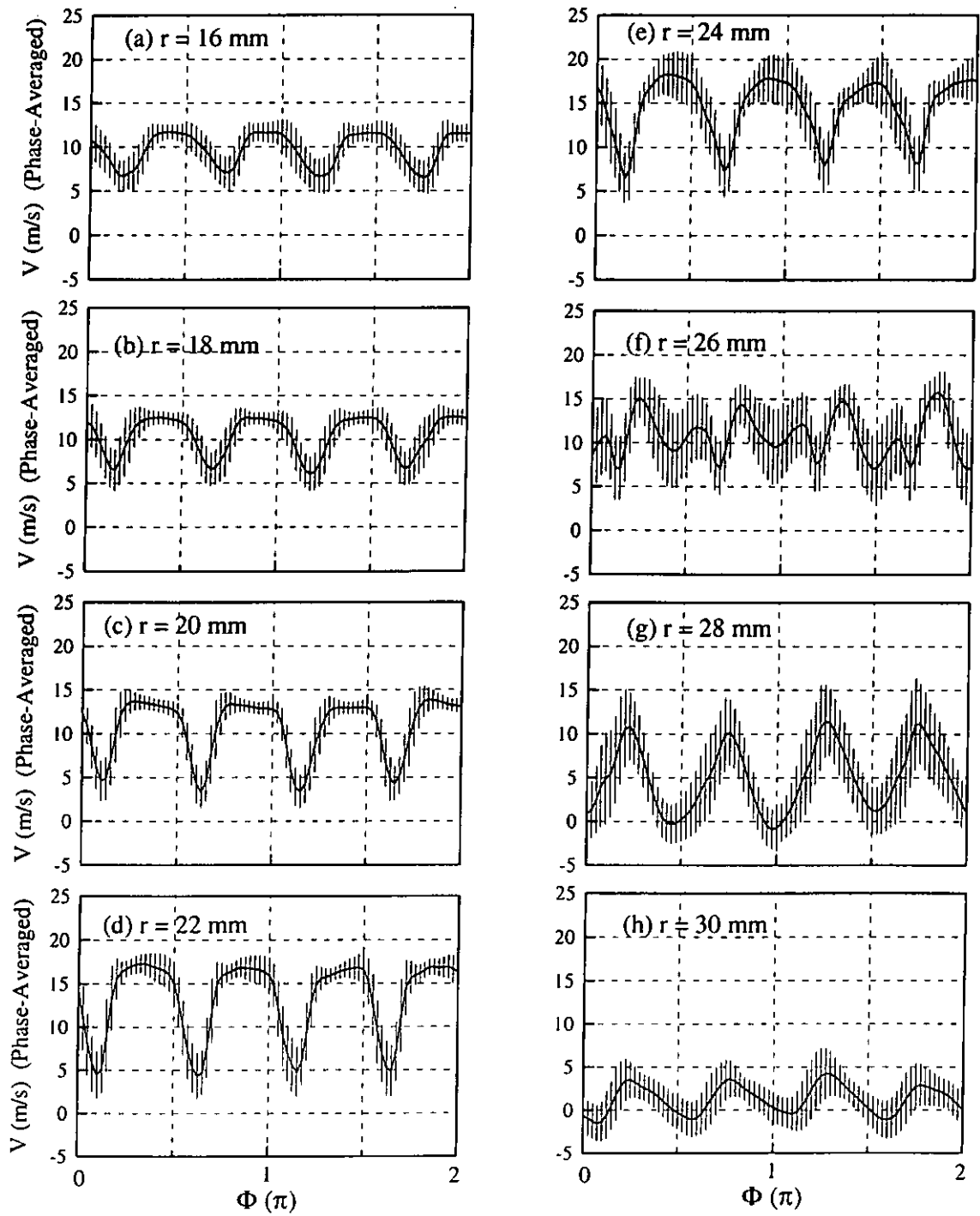


Figure 2.7: Distribution of local average of the circumferential velocity and its standard deviation.

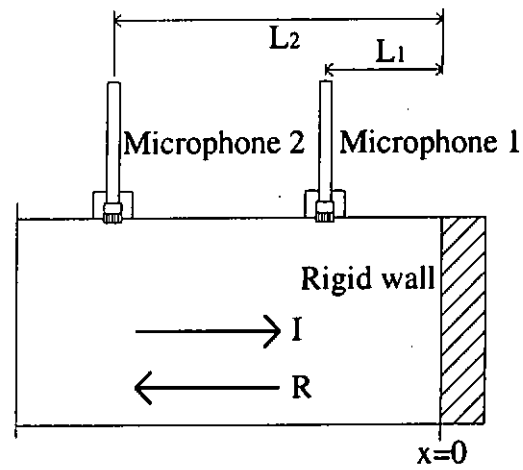


Figure 3.1: The schematic diagram of microphone calibration.

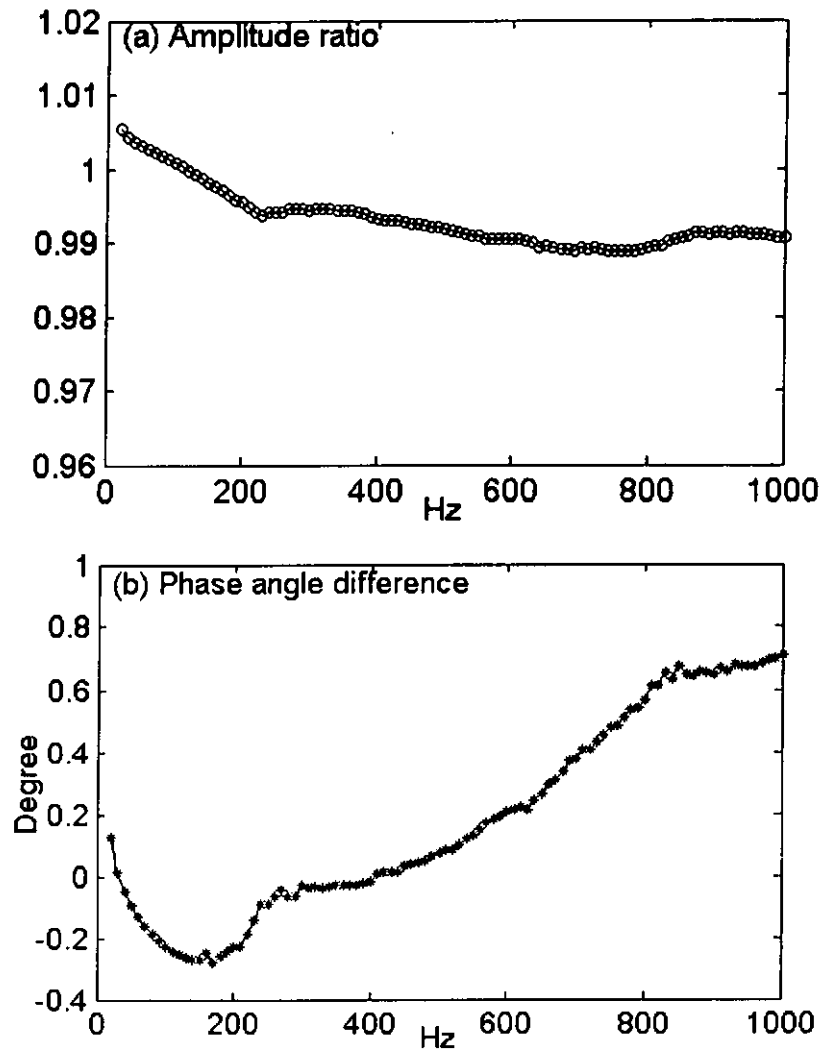


Figure 3.2: The results of microphone calibration by the microphone-swapping method inside a duct. (a) is the amplitude ratio and (b) is the phase angle difference.

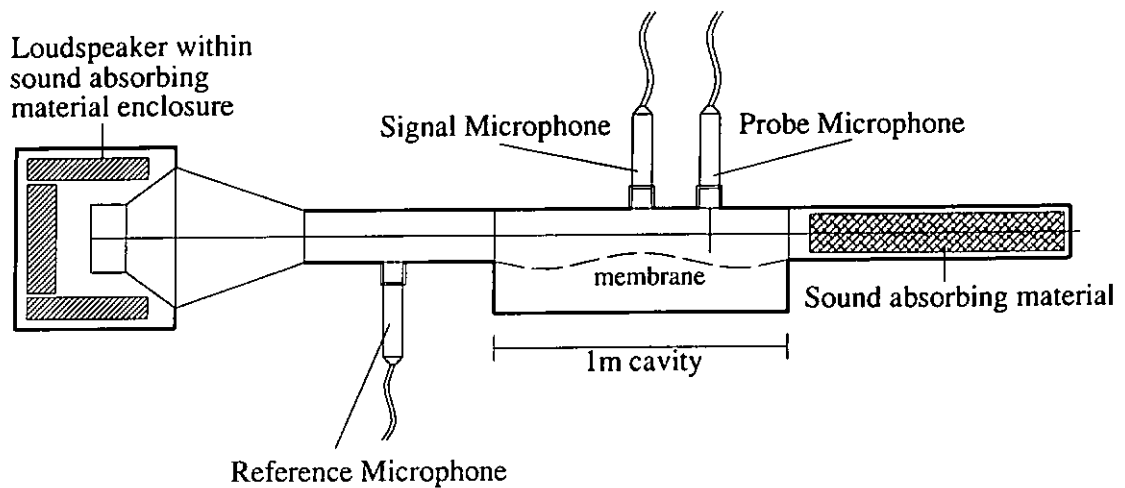


Figure 3.3: The experimental set-up for the duct acoustics project.

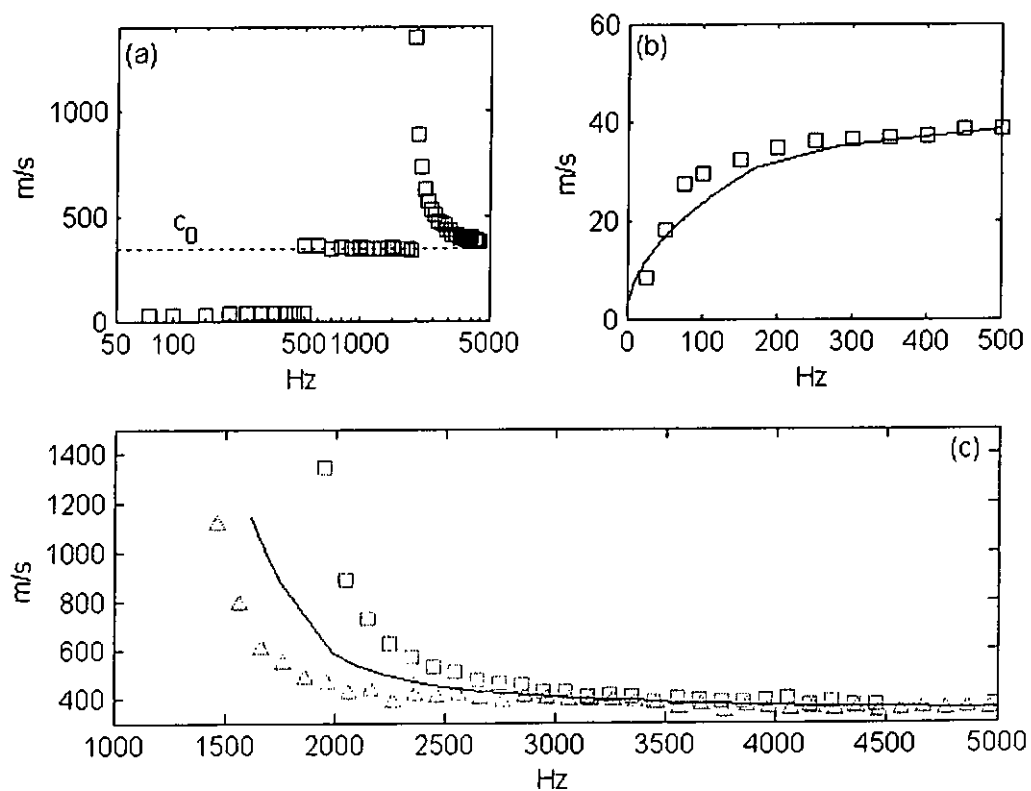


Figure 3.4: The comparison of theoretical prediction (solid curves) and experimental data (open squares) of the dispersion relation for sound propagation through a duct with one flexible wall. The experiment were conducted by the chirp sound source. (a) is the experimental data over the whole frequency range, (b) and (c) are, respectively, the zoom-in views of the data compared with theoretical predictions for the two frequency regions in which the wave speed is subsonic and supersonic.

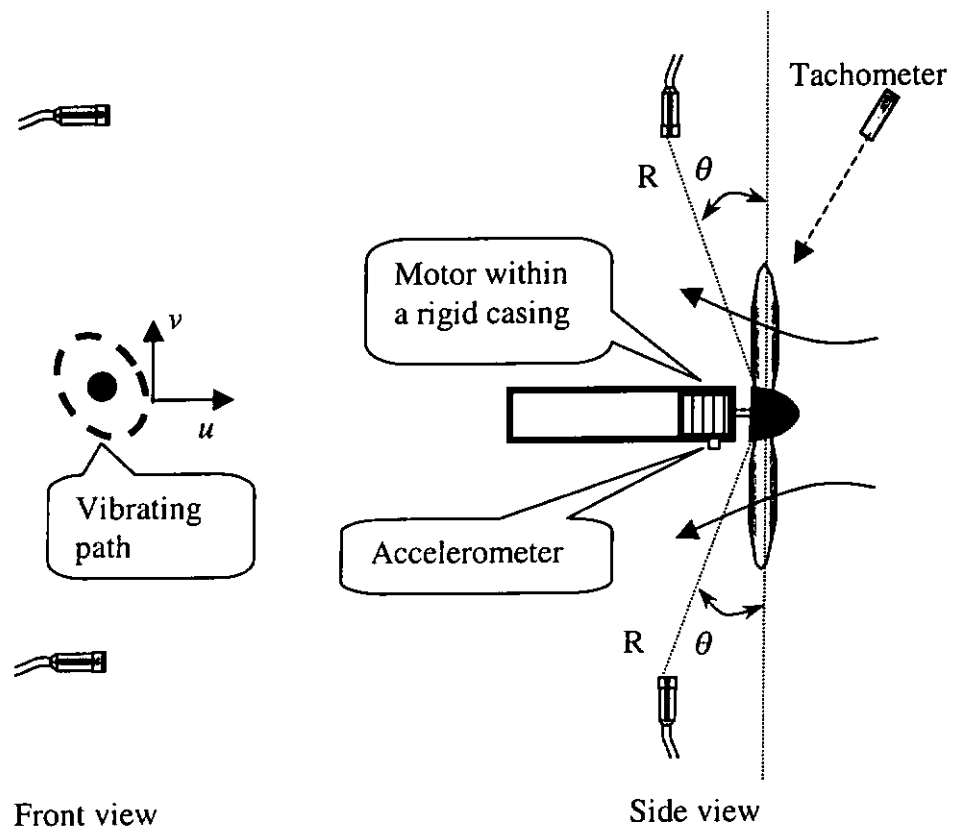


Figure 3.5: The schematic diagram of the experiment.

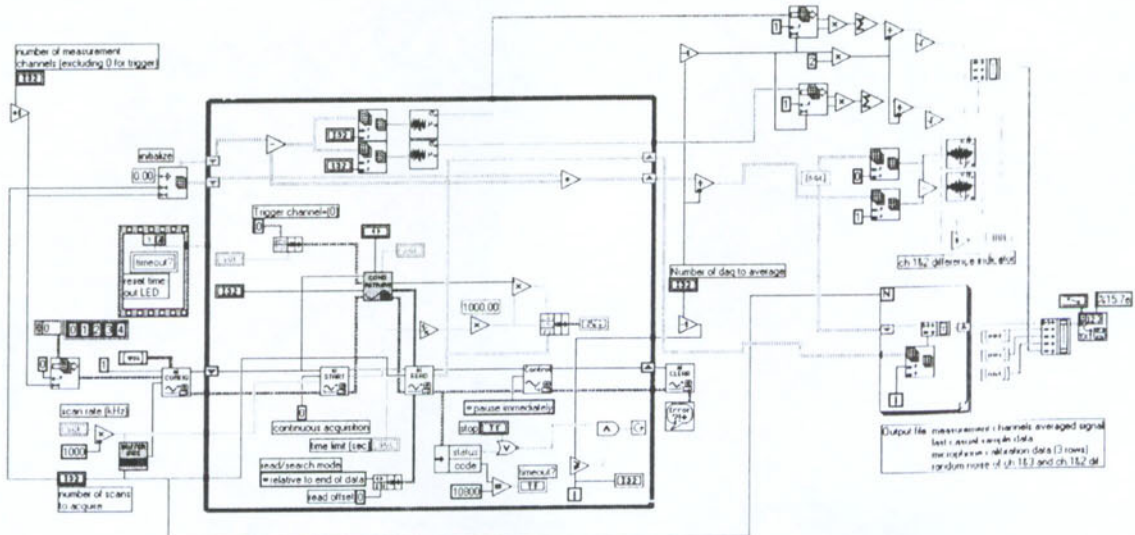
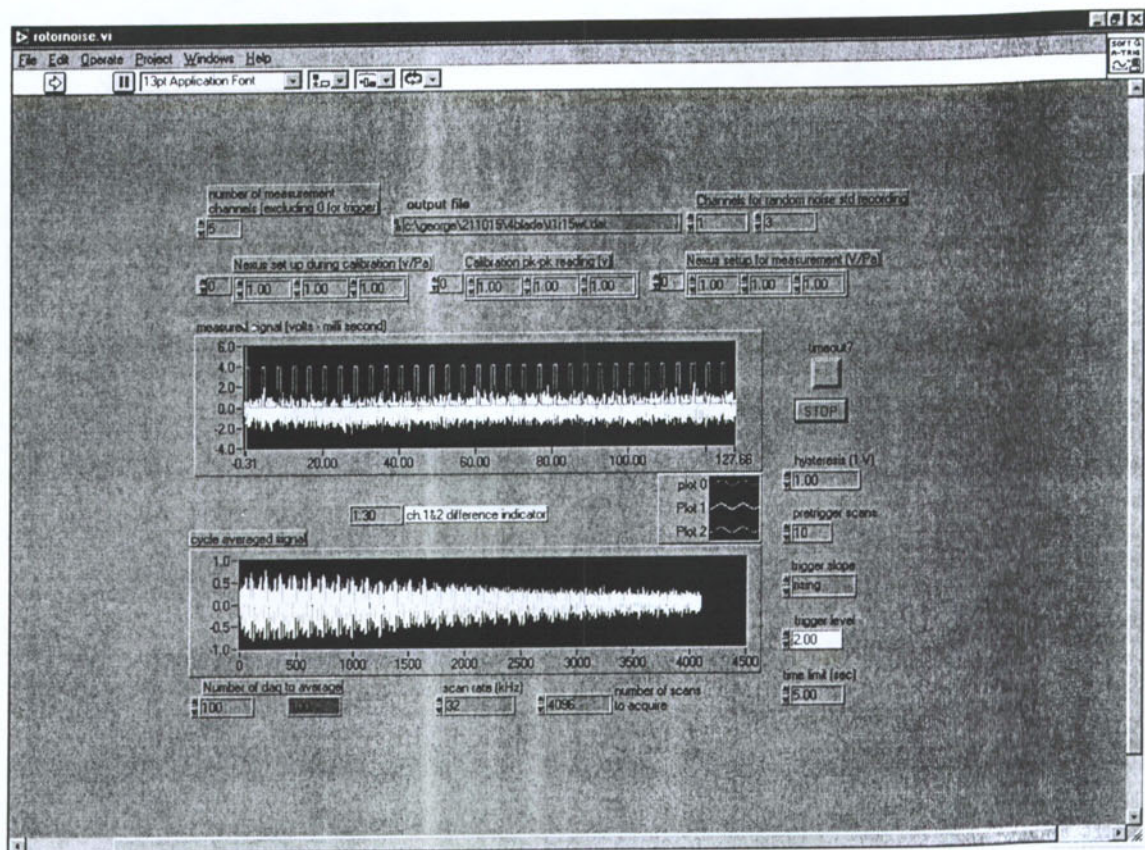


Figure 3.6: The LabVIEW code controlling the data acquisition process. The top is the front panel and the lower picture is the diagram of the code.

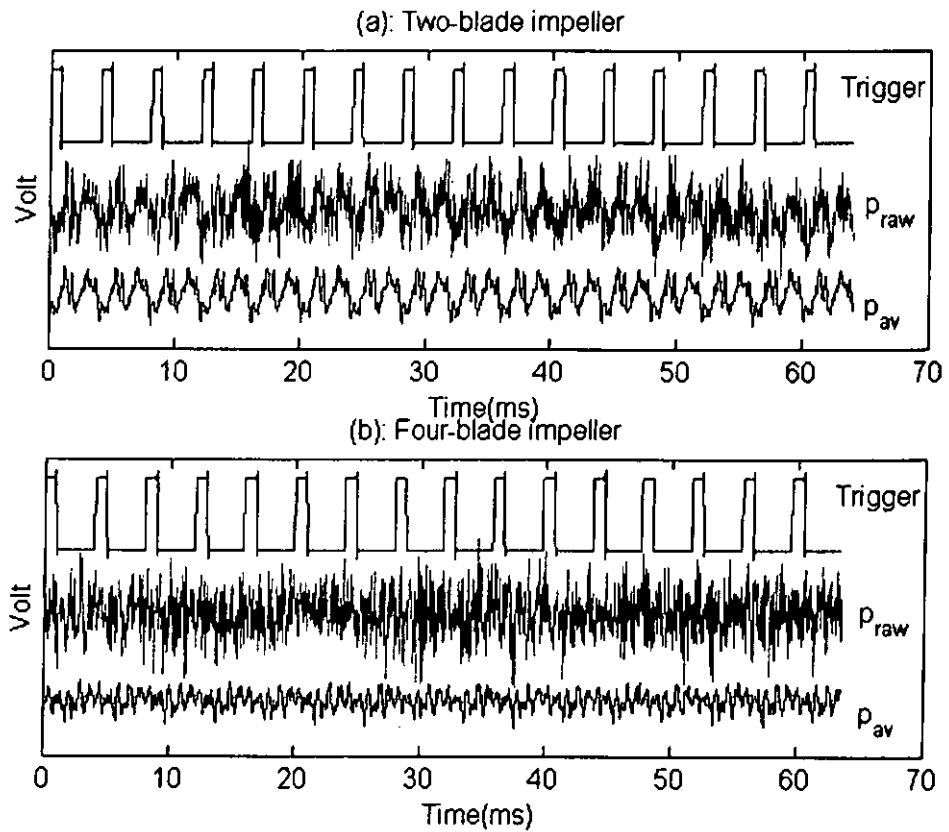


Figure 3.7: Example of the tachometer-triggered data acquisition. One record has 16 cycles. Noise is measured at 120 deg from the rotating axis at distance 0.6m. The rotational speed is 15000rpm for both cases.

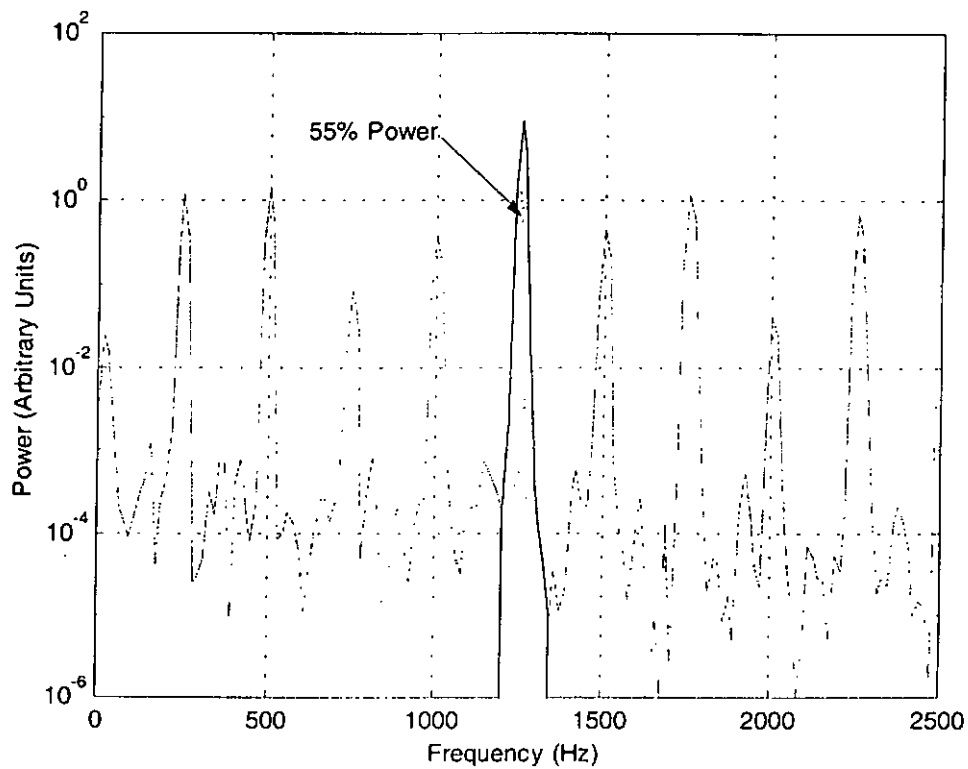


Figure 3.8: Motor noise spectrum.

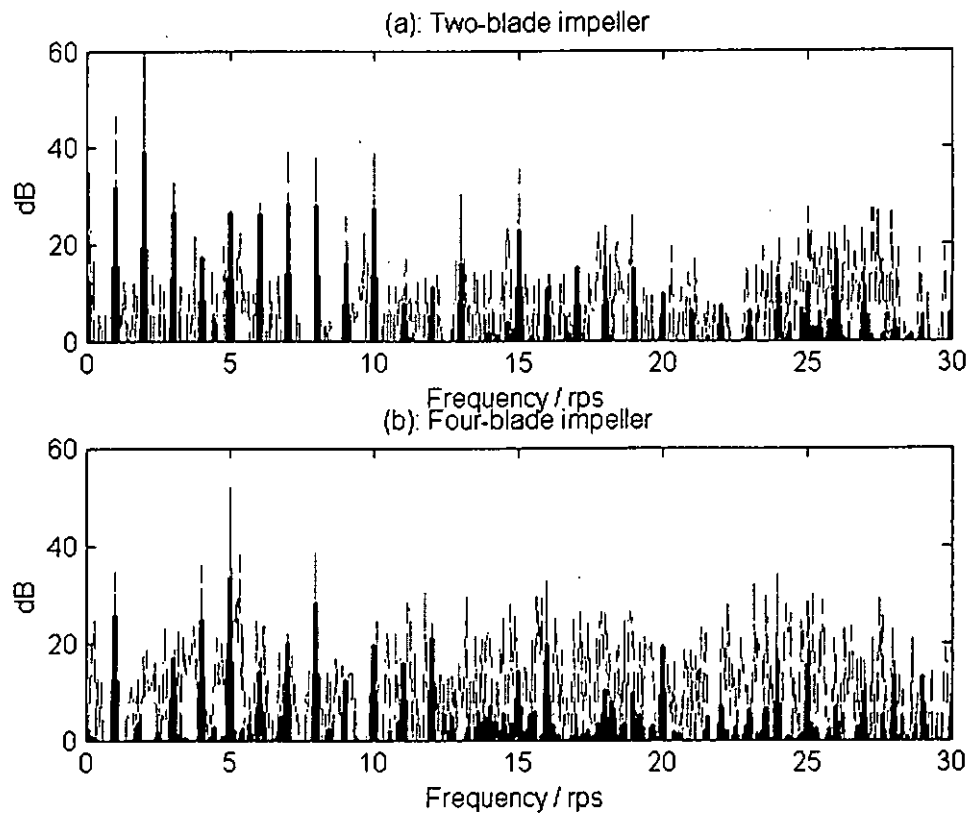


Figure 3.9: Spectra of sample data shown in Figure 3.7. The dashed curves are for the raw data and the thick solid curves for the averaged data.

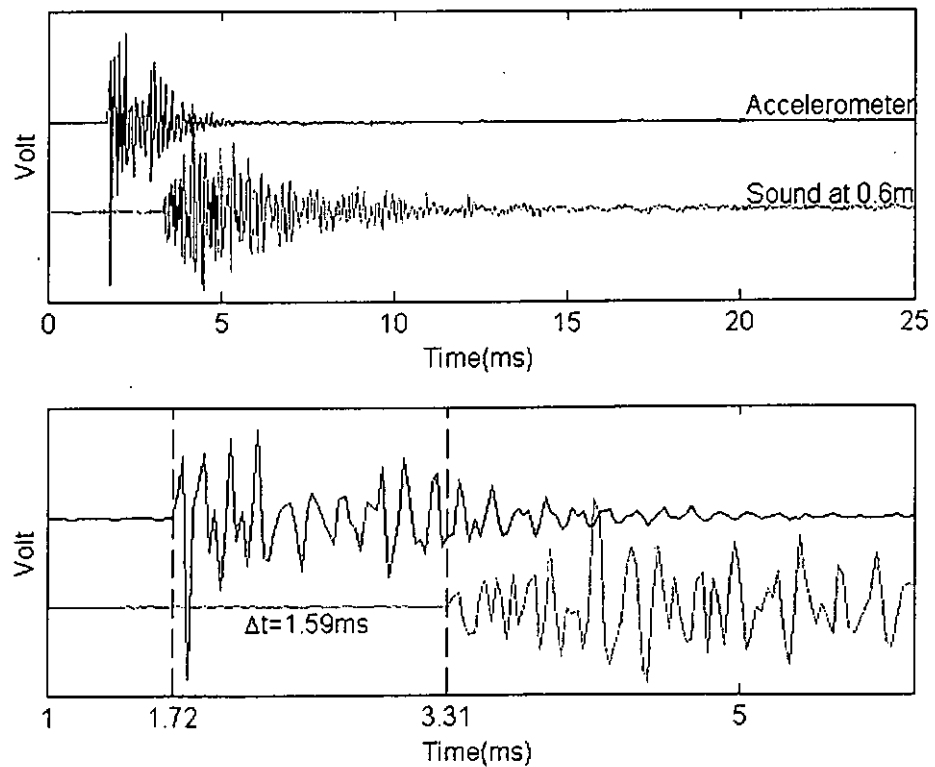


Figure 4.1: Signals from the striking test using a sampling frequency of 32kHz.

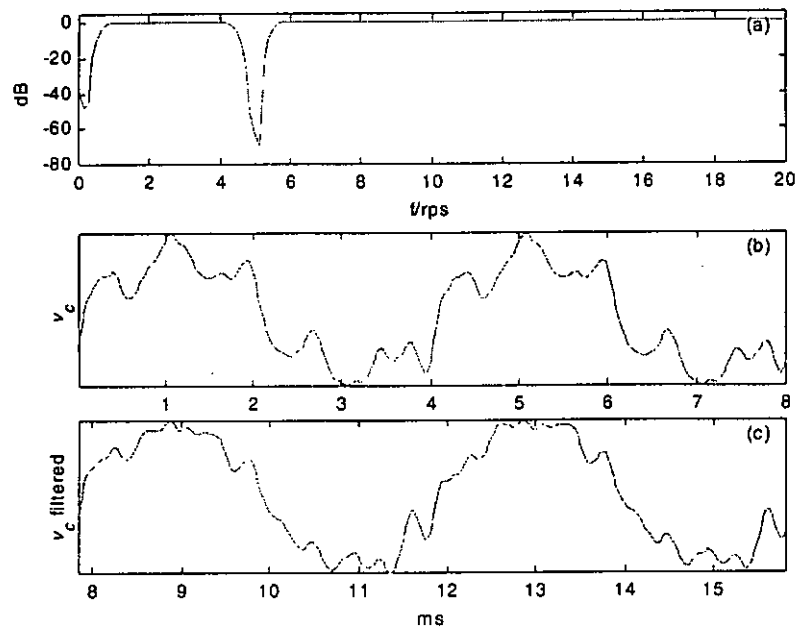


Figure 4.2. FIR filtering of the signals to exclude the low-frequency drifting and the motor brush induced vibration and noise at the 5th harmonic of the shaft rotational speed. (a) is the amplitude of the finite impulse response, (b) is the vibration velocity signal with synchronous averaging before filtering, (c) is the vibration velocity in (b) after filtering.

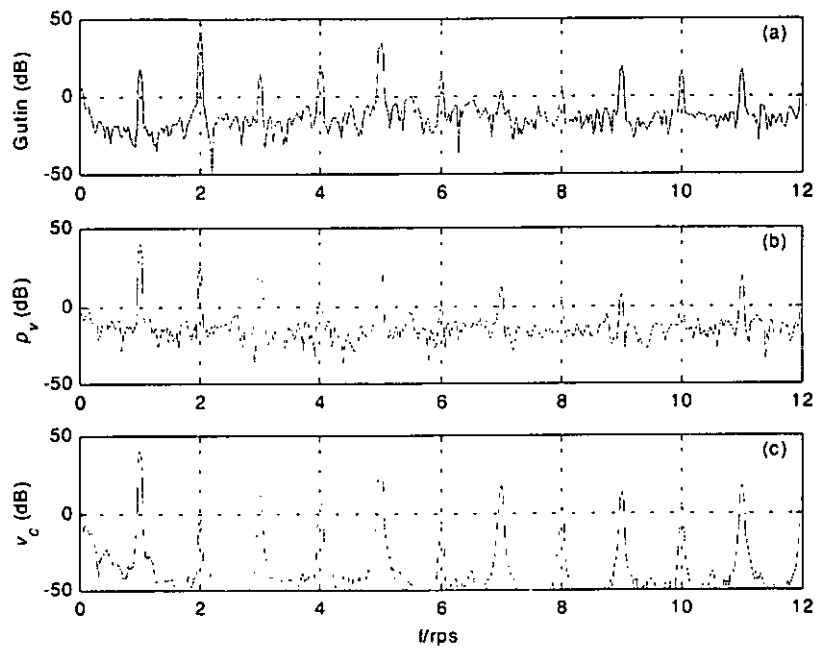


Figure 4.3: Spectral comparison for (a) the averaged Gutin noise, p_g , and (b) the averaged vibration noise, p_v , and (c) the casing vibration signal v_c .

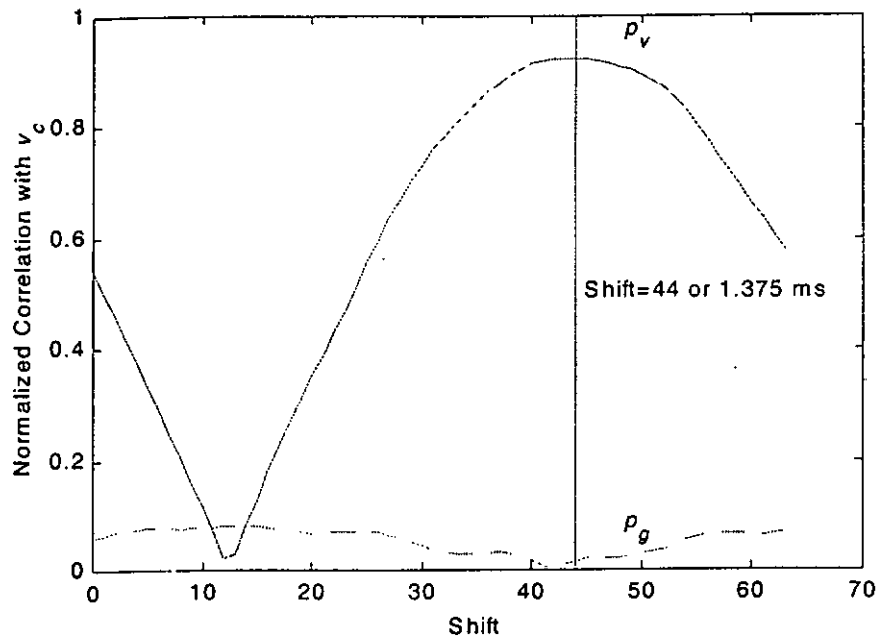


Figure 4.4: Normalized correlation as a function of the shift index of the signals between sound and vibration. The solid line is for correlation between p_v and v_c , and the dashed line is between p_g and v_c . The maximum correlation (0.924) is found with a shift of 44 data points.

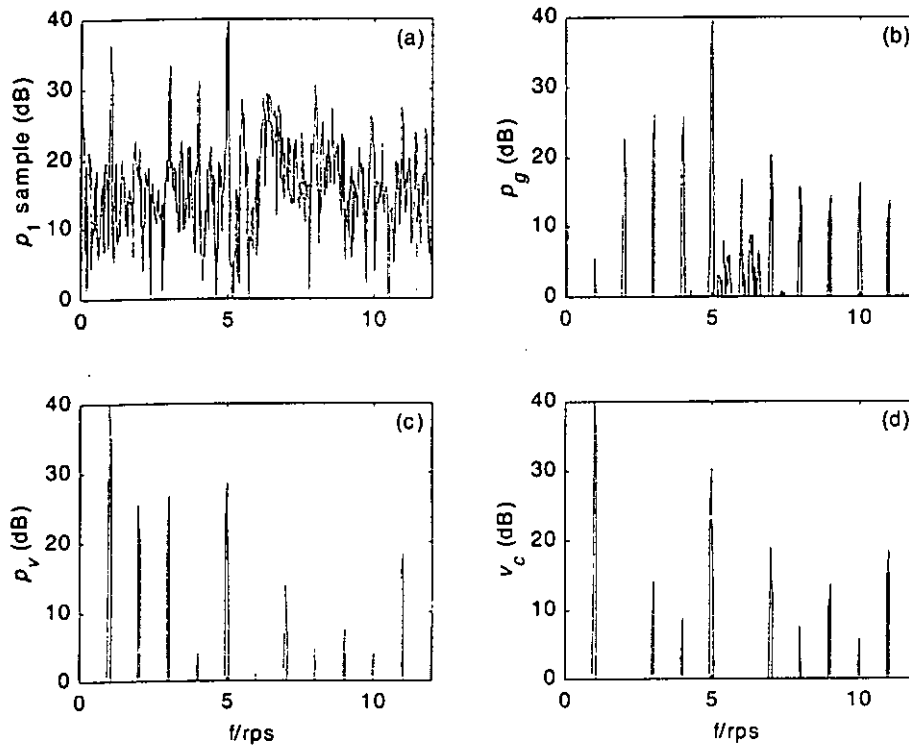


Figure 4.5: Spectral comparison of a four-blade fan. (a) Raw aerodynamic noise p_l ; (b) averaged Gutin noise p_g ; (c) averaged vibration noise p_v ; (d) averaged casing vibration v_c .

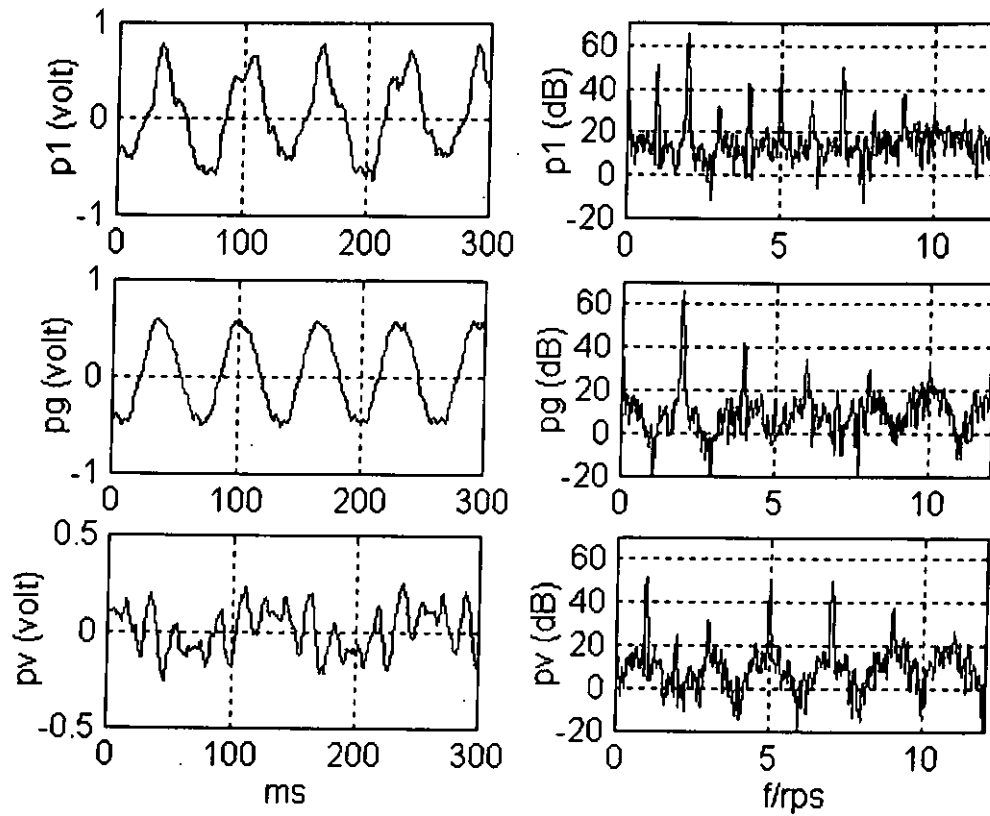


Figure 4.6: Analysis of the 2-blade impeller by the one-microphone method.

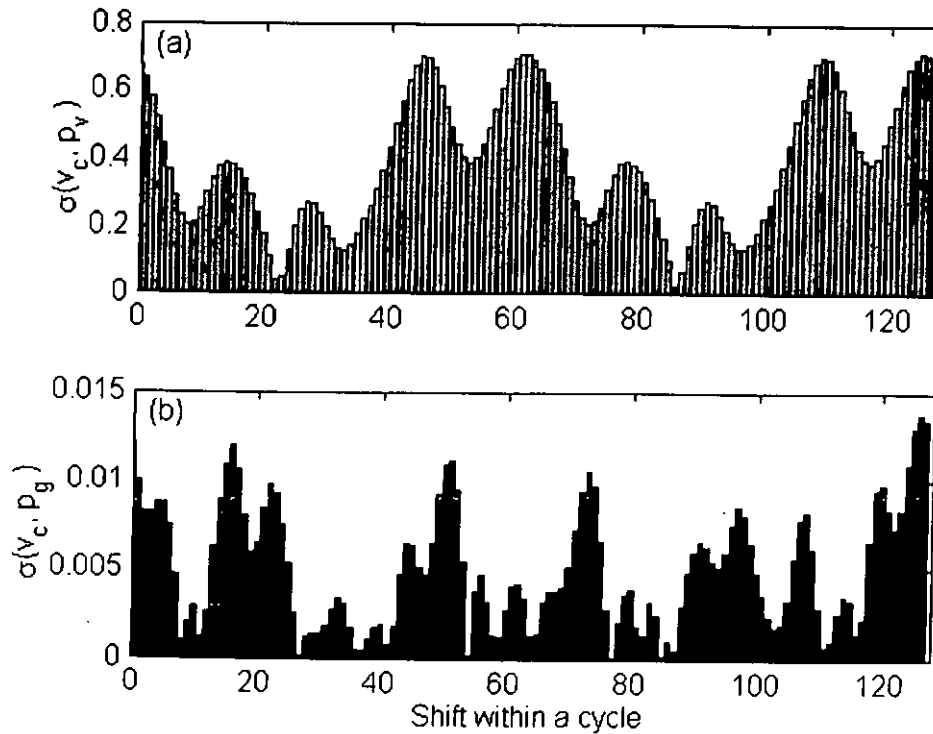


Figure 4.7: The correlation indices of the Gutin and vibrational noise with the accelerometer signal for the 2-blade impeller.

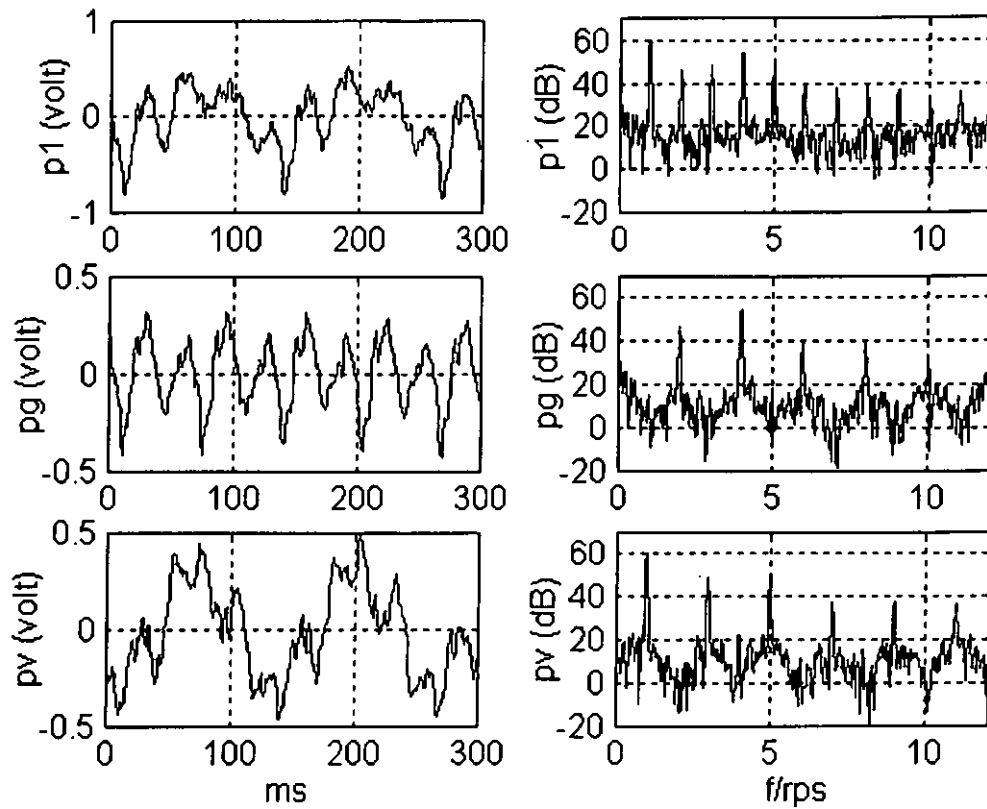


Figure 4.8: The signals from the 4-blade impeller analysed by the one-microphone method.

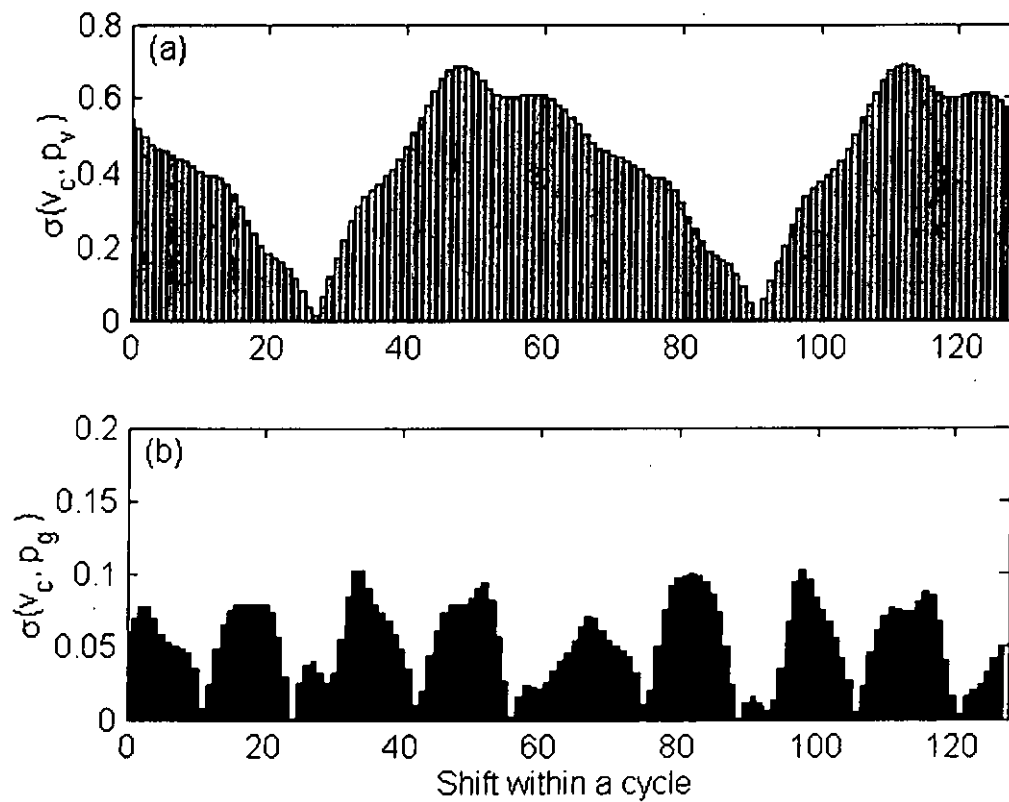


Figure 4.9: The correlation indices of Gutin and vibrational noise with the accelerometer signal for the 4-blade impeller.

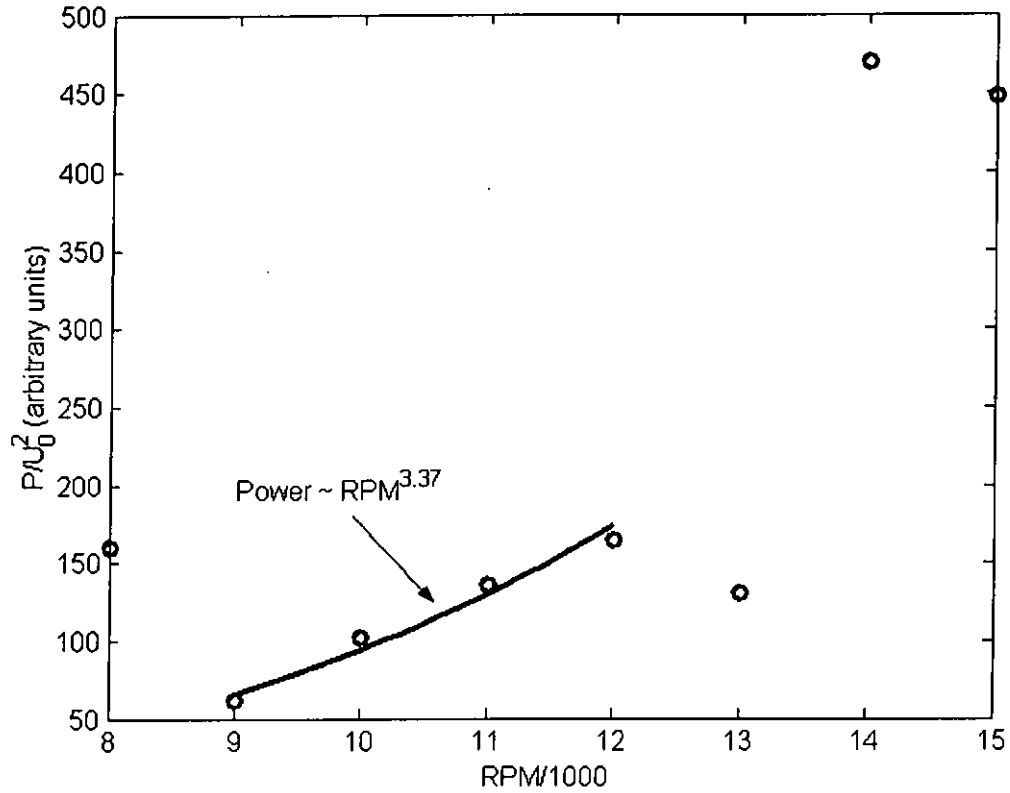


Figure 4.10: The study of the cubic power law for the vibrational noise radiation.

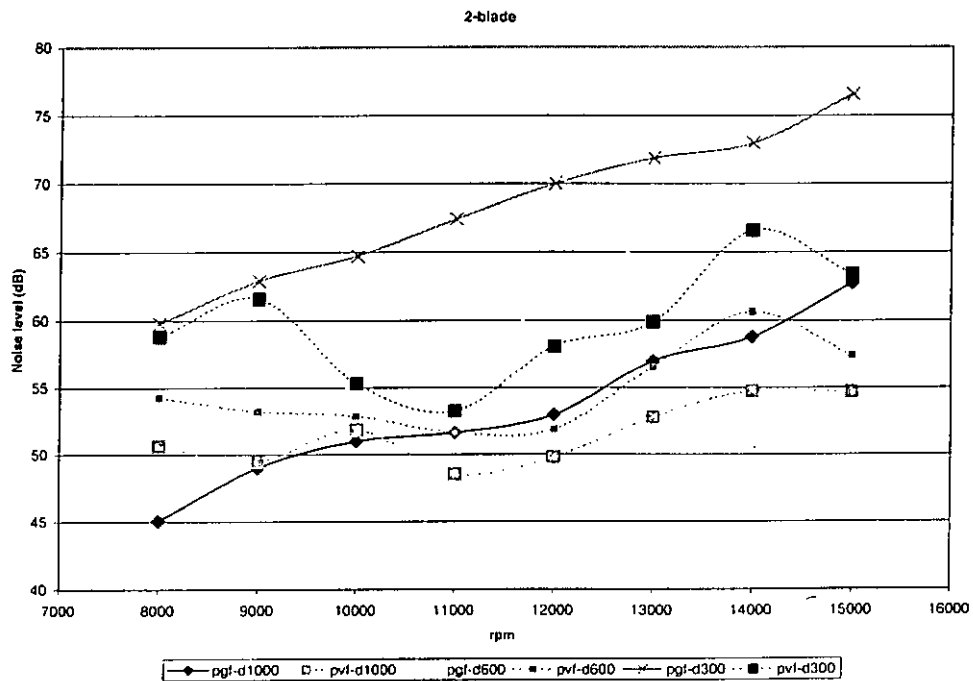


Figure 4.11: The comparison of Gutin and vibration noise for the 2-blade impeller. Legends: p_g means Gutin noise pressure, p_v means vibrational noise, f means that the brush noise at 5rps is filtered, d600 means measured at a distance of $R=600\text{mm}$.

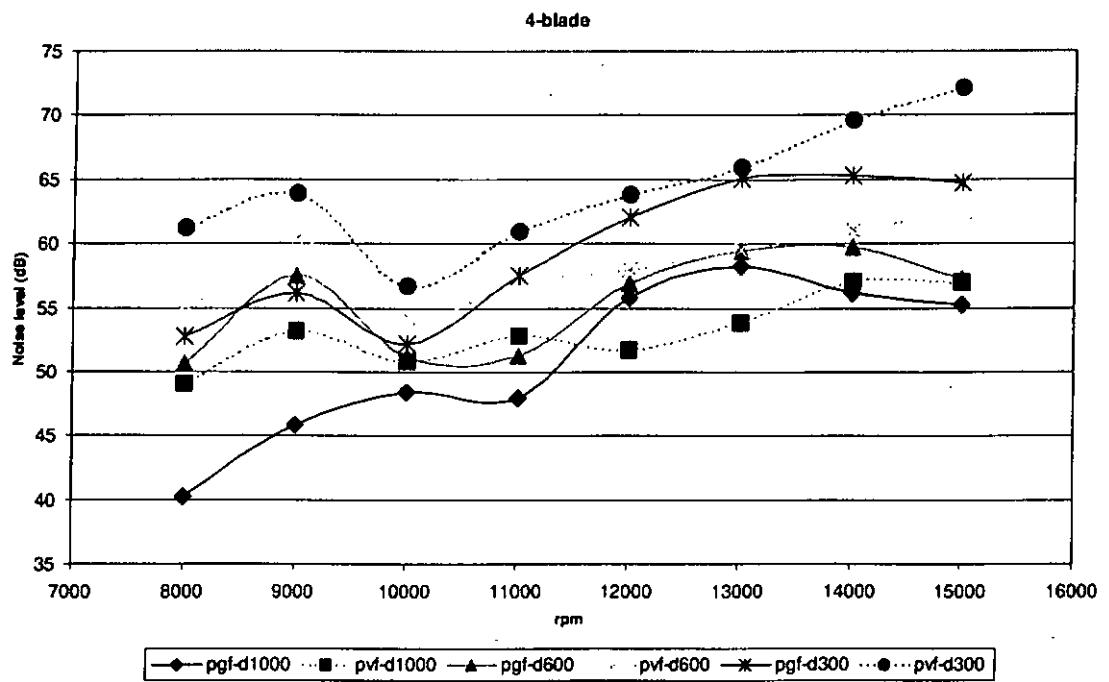


Figure 4.12: The comparison of Gutin and vibration noise for the 4-blade impeller.

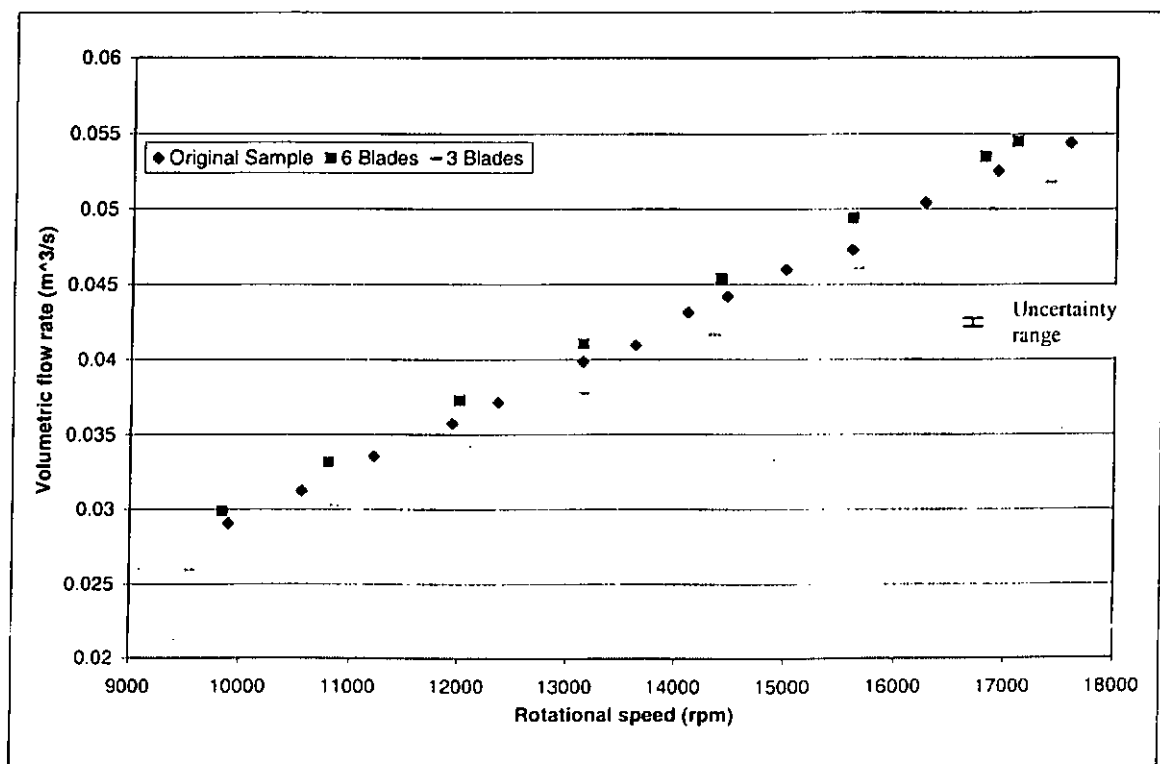


Figure 5.1: The volumetric flow rate for different number of guide vanes.

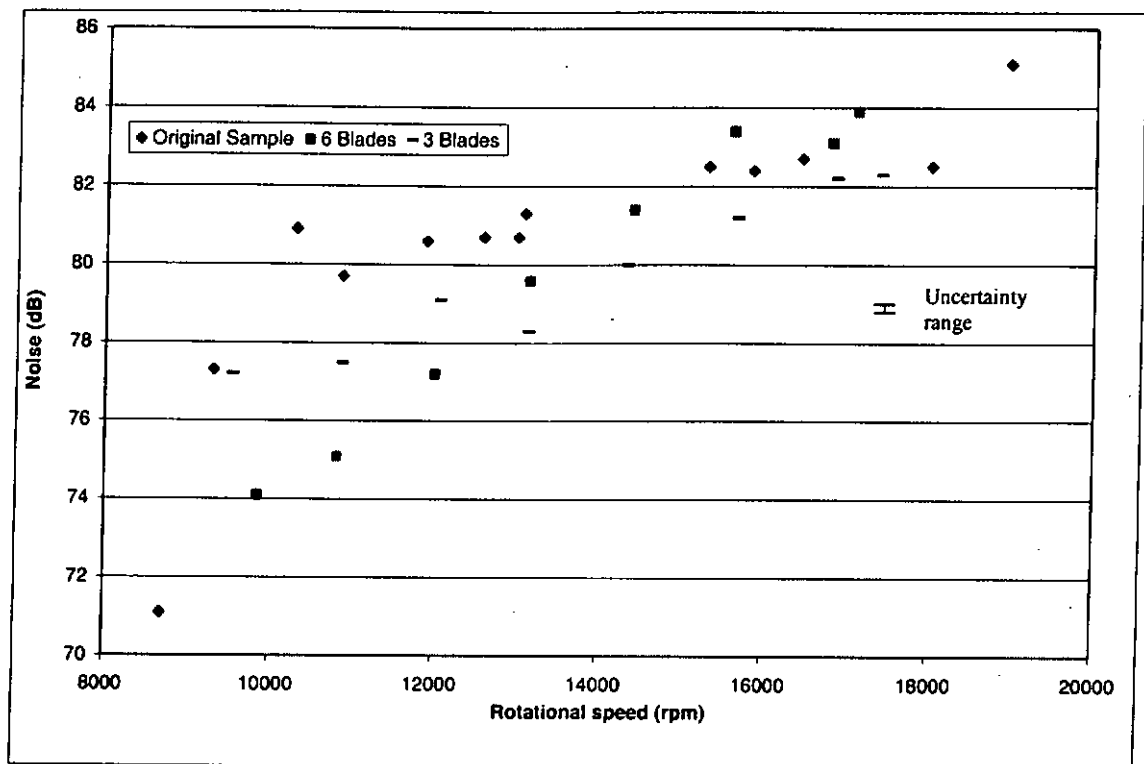


Figure 5.2: The variation of the near field noise with respect to the number of guide vanes.

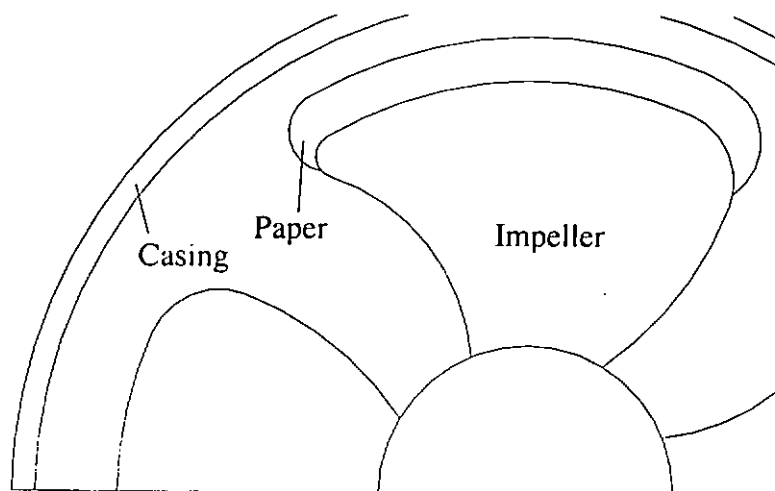


Figure 5.3: The schematic diagram of tip clearance modification by adding paper.

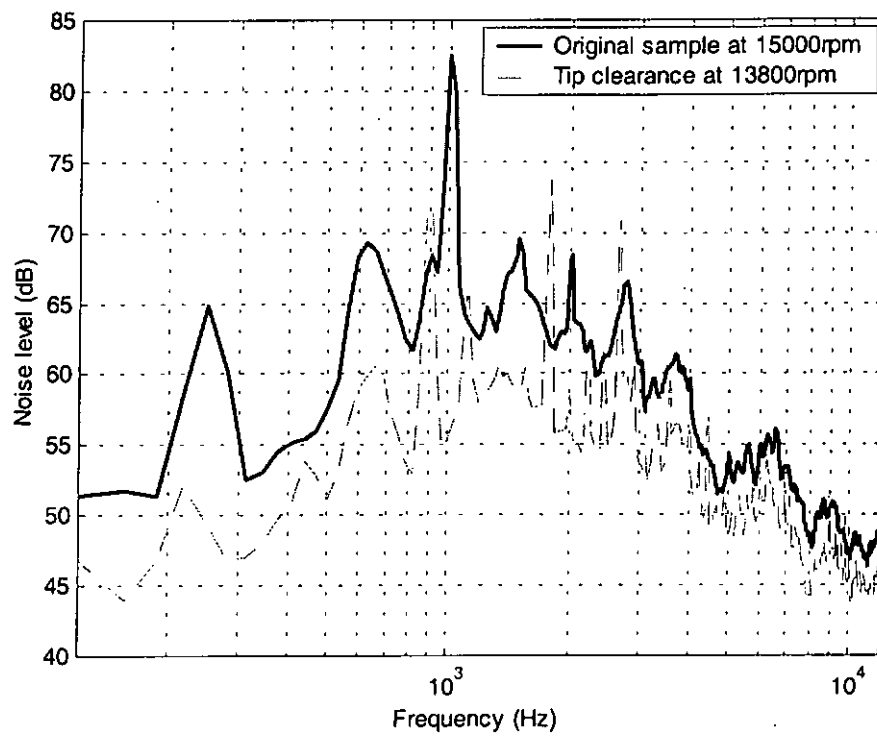


Figure 5.4: Narrow-band spectral comparison between the original sample and modified impeller with smaller tip clearance.

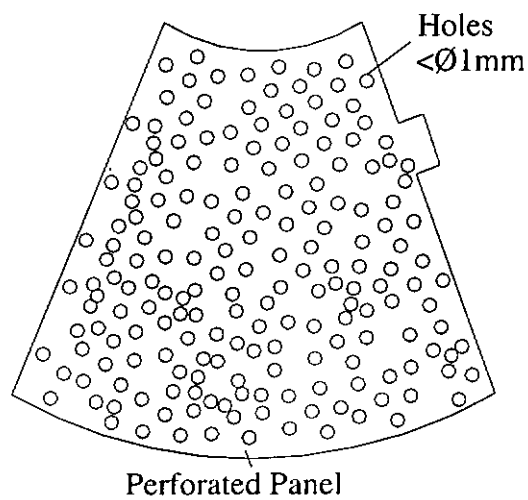


Figure 5.5: The design of perforated panel for use inside the fan casing.

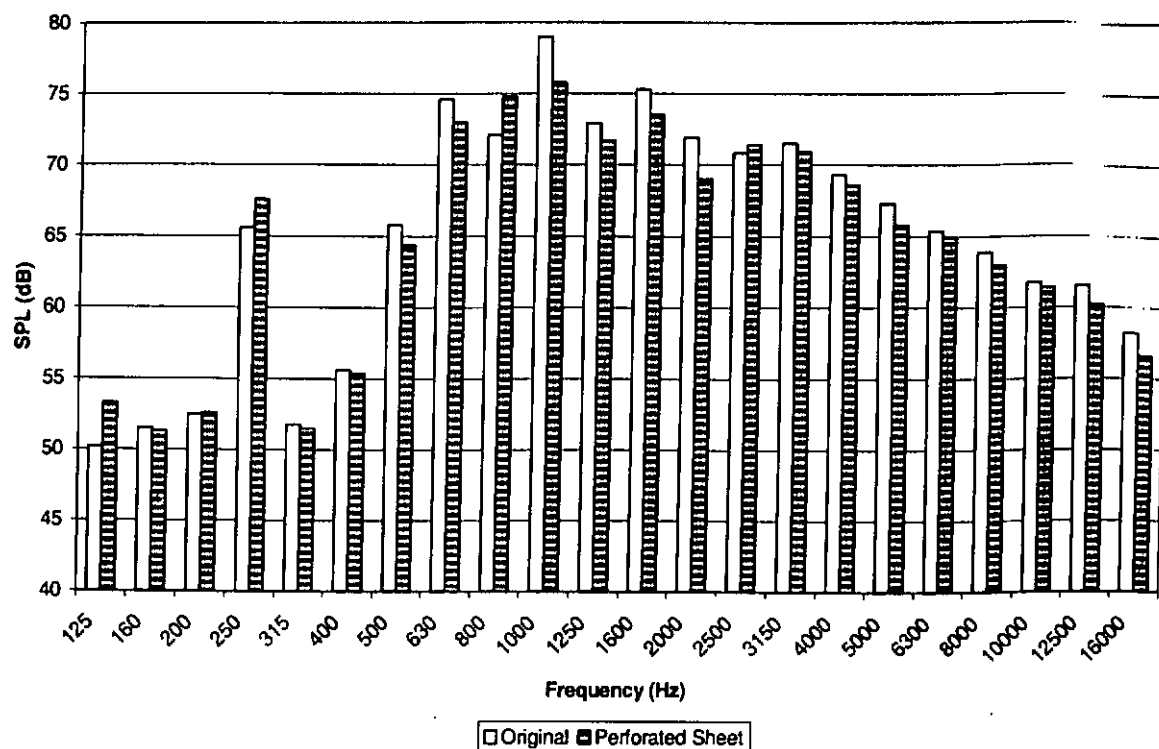


Figure 5.6: The comparison of noise with and without the perforated casing.

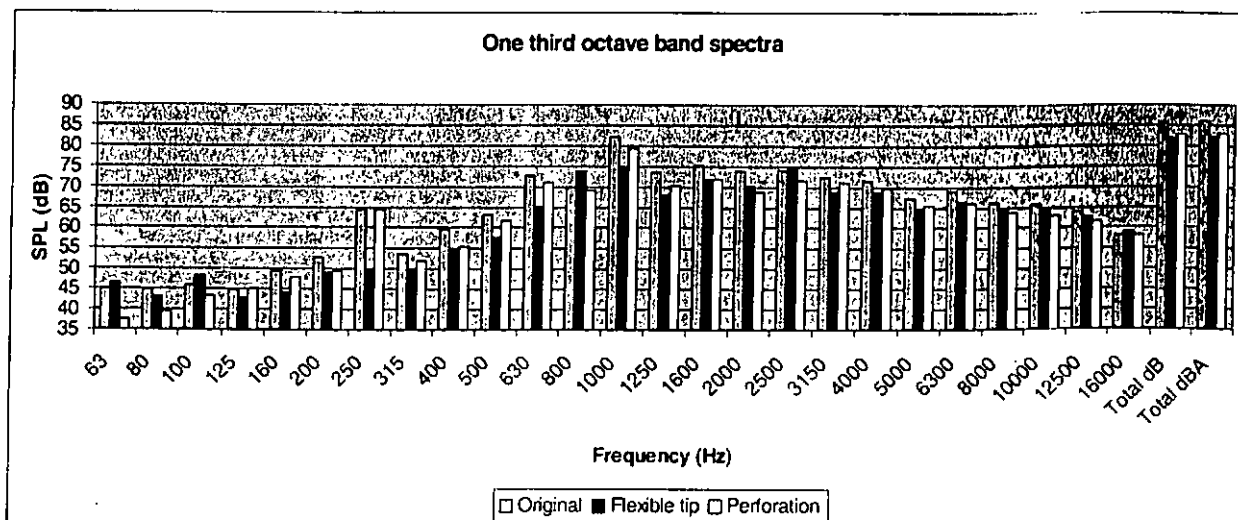


Figure 5.7: One-third octave band comparison of the original fan with two successful measures of modifications.